PHYSICAL REVIEW D

PARTICLES AND FIELDS

THIRD SERIES, VOLUME 34, NUMBER 1 1 JULY 1986

Measurement of spin-spin correlation parameters in the p-p system at 11.75 GeV/c

I. P. Auer,[a] E. Colton,[b] W. R. Ditzler,[c] H. Halpern,[d] D. Hill, H. Spinka, N. Tamura,[e] J. -J. Tavernier,[f] G. Theodosiou,[g] K. Toshioka,[h] D. Underwood, R. Wagner, Y. Watanabe,[i] and A. Yokosawa

High Energy Physics Division, Argonne National Laboratory, Argonne, Illinois 60439

(Received 17 January 1986)

Final results are presented of the proton-proton elastic-scattering spin parameters $C_{SS}=(S,S;0,0)$ and $C_{LS}=(L,S;0,0)$ for $\theta_{\text{c.m.}}=8°$–$49°$ and of $C_{LL}=(L,L;0,0)$ for $\theta_{\text{c.m.}}=8°$–$90°$ at 11.75 GeV/c. Comparisons to theoretical models are also made.

I. INTRODUCTION

Final results are presented in this article for spin-spin correlation parameters in pp elastic scattering at 11.75 GeV/c. These measurements were obtained with a polarized beam from the Argonne Zero Gradient Synchrotron (ZGS) and a polarized target. Both the beam and target were polarized in the horizontal scattering plane, and the spin of the outgoing protons was not measured.

With a polarized beam and/or target, the only nonzero pp elastic-scattering observables are the polarization or analyzing power P, and the four spin-spin correlation parameters C_{NN}, C_{LL}, C_{SS}, and $C_{LS}=C_{SL}$. The spin directions are **N** (normal to the scattering plane with the forward particle to beam-left), **L** (longitudinal along the beam direction), and $\mathbf{S}=\mathbf{N}\times\mathbf{L}$. In the notation $(B,T;F,R)$, where B is the beam, T is the target, F is the forward scattered, and R is the recoil spin direction, then

$$P=(0,N;0,0)=(N,0;0,0)\ ,$$

$$C_{NN}=(N,N;0,0)\ ,$$

$$C_{SS}=(S,S;0,0)\ ,$$

$$C_{LS}=(L,S;0,0)=C_{SL}=(S,L;0,0)\ ,$$

$$C_{LL}=(L,L;0,0)\ ,$$

where 0 denotes unpolarized or no measurement of the spin.

The data reported here are for C_{SS} and C_{LS} from $\theta_{\text{c.m.}}\sim 8°$–$49°$ or four-momentum transfer squared $-t\sim 0.2$–3.5 (GeV/c)^2 and for C_{LL} from $\theta_{\text{c.m.}}\sim 8°$–$90°$ or $-t\sim 0.2$–10.2 (GeV/c)^2 for pp elastic scattering. Additional measurements of C_{SS} and C_{LS} to larger angles were not performed because of lack of accelerator time and interference of the polarized-target magnet coils with the desired aperture. Most of the elastic-scattering results were taken in three overlapping angular regions to optimize the beam intensity and to allow for the steeply falling differential cross section. This also permitted a comparison of data in the overlap region.

This paper is organized into six sections. The experimental apparatus is described in Sec. II and the data analysis in Sec. III. Pure spin parameters are extracted from the measurements in Sec. IV. The results show significant spin effects in both C_{SS} and C_{LL} at intermediate and large angles. The parameters P and C_{NN} have also shown large effects.[1–9] The combined information from all spin measurements at 11.75 GeV/c is used to try to understand these effects in a model independent way in Sec. V. A comparison to various model predictions is also given for the small-angle data and the results near 90° c.m. Finally, a summary and conclusions are presented in Sec. VI. The C_{LL} data near 90° have been published previously in a short paper.[10]

II. EXPERIMENTAL APPARATUS

A. The polarized beam

Polarized protons from a ground-state atomic-beam polarized ion source were accelerated to 750 keV in a Cockcroft-Walton accelerator, then to about 50 MeV in a linear accelerator, and finally they were injected into the Zero Gradient Synchrotron[11,12] (ZGS). The protons were accelerated and then resonantly extracted from the ZGS. For this experiment, the beam extraction period (flattop) was roughly 0.7 s and the beam pulses occurred every 3.8 s during most of the measurements at the beam momentum of 11.75 GeV/c. The polarized protons were then transported down the external proton beam line (EPB 1). At several points, thin septum magnets split the beam from EPB 1 for use in individual beam lines by various experiments.

The beam polarization was measured before injection into the ZGS with the 50-MeV polarimeter.[11–14] It was monitored after acceleration with the CERN polarimeter.[14] During the analysis of these experiments, the CERN calibration was adjusted slightly to give the same average beam polarization as measured by an absolute polarimeter[14] in our beam line. The beam was nominally N type (transversely polarized in the vertical direction) with a typical polarization between 55% and 65% at 11.75 GeV/c.

A new beam line (beam 22) was constructed specifically for this experiment.[15] An earlier beam line (beam 22B) (Refs. 16 and 17) had been used by our group for a number of earlier polarized-beam experiments at lower energies,[18–25] but it was restricted to particle momenta below 6.5 GeV/c. The new beam line, shown in Fig. 1, could transport particles with momenta up to 12 GeV/c.

A portion of the polarized proton beam was split from EPB 1 using three thin septum magnets SB1–SB3. The pulsed septum magnet SB1 actually consisted of four identical magnets in series. In addition, several other bending magnets and quadrupoles were used to bring the polarized beam to a focus near a liquid-hydrogen (LH_2) target. An absolute beam polarimeter,[14] which measured only the N-type component of the beam spin, was installed in the beam line utilizing this LH_2 target. The beam spot size at the LH_2 target [typically 6–10 mm full width at half maximum (FWHM)] depended on the location of a 33-cm-long uranium collimator located immediately upstream of SB1, which in turn depended somewhat on the desired beam intensity. For most runs, the beam polarization was taken from this polarimeter. For runs where this polarimeter was not operational, the CERN-polarimeter results were used.

Following the LH_2 target were several more bending magnets and quadrupoles, plus two superconducting solenoids. These magnets were used to precess the beam spin direction from N to L type (longitudinal polarization) or S type (transverse polarization in the horizontal plane) and to refocus the beam at the polarized proton target (PPT). Two small vernier steering magnets, ST1 and ST2, were also used to vertically center the beam on the PPT. A number of magnets (Q5 to solenoid B) had to be moved in order to change the spin direction at the PPT from S to L type; for additional details see Ref. 15.

The superconducting solenoids were quite similar in construction, with a 11.4-cm inside diameter (cold bore) for the beam. They consisted of 21 870 turns of superconductor over a winding length of 178 cm with two iron end pieces, each 7.6 cm long. Each was designed to precess a 6-GeV/c proton spin by 90°, which requires $\int B\,dl = 11.3$ T m. To achieve this required a current of 410 A; the corresponding central field was about 6.7 T. The measured uniformity of $\int B\,dl$ over the cold bore for one of the magnets was better than 4%. The liquid-^{4}He consumption of the solenoids was about 3 and 8 l/hr.

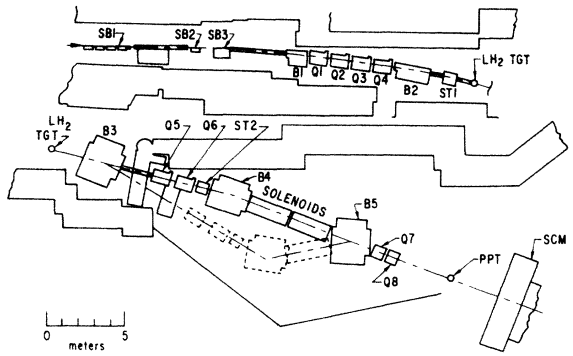

FIG. 1. Layout of the beam line used for this experiment. Septum magnets SB1–SB3 split the polarized beam from the main external proton beam-line EPB 1. Additional bends occurred in dipoles B1–B5, and vernier vertical steering magnets ST1 and ST2. Focusing was performed in the quadrupoles Q1–Q8 at the intermediate focus near the liquid-hydrogen target (LH_2 TGT), and the polarized proton target (PPT). The configuration shown had B5 turned off and an S-type beam at the PPT. A move of magnets Q5, Q6, ST2, and B4, and the solenoids, toward the magnet locations with dashed lines, was needed to obtain an L-type beam; in that case B5 was turned on.

The observed beam spot near the PPT was roughly 19 mm FWHM horizontally and 12 mm FWHM vertically (see Table I). The spot size was dominated by the size of the collimator near SB1 and by multiple scattering in the LH_2 target and various vacuum windows. The average beam divergences at the PPT were 7.4 mrad FWHM horizontally and 4.2 mrad FWHM vertically. The divergences were limited by various magnet apertures and by a 20-cm-long circular brass collimator located between Q5 and Q6. At low beam intensities, the incident beam trajectories were measured with three multiwire proportional

TABLE I. Measured beam properties at the polarized target. The beam-spot size and beam divergence (FWHM) at the polarized target were measured with the three MWPC's located in the beam, upstream of the target. Data are missing for certain configurations because these chambers were turned off during high-intensity runs.

Configuration	Spot size (mm)		Divergence (mrad)	
	Horizontal	Vertical	Horizontal	Vertical
Low $-t$ C_{SS}	22	11	8.8	3.8
Low $-t$ C_{LS}	16	13	7.0	4.6
Low $-t$ C_{LL}	12	12	5.8	3.4
Medium $-t$ C_{LS}	26	12	9.1	4.4
Medium $-t$ C_{LL}	14	9	6.2	4.1
High $-t$ C_{SS} (run 2)	22	12	7.5	5.2

chambers (MWPC's) located upstream of the PPT. At higher beam intensities, these chambers were turned off because their performance was degraded by the high rates. The beam intensities at the PPT ranged from 2×10^5 to 2×10^7 polarized protons per 0.7-s spill, depending on the elastic-scattering angles being measured.

Beam steering was monitored using segmented proportional ion chambers (SPIC's) located at several points along the beam line, and with scintillation counters and MWPC's near the polarized target. Attempts were made to carefully steer the beam along the axis of the solenoids; in practice some beam steering occurred in the solenoids. The $\int B\,dl$ of the final bending magnet (B5) was well known from Hall probe and wire-orbit measurements. Estimates of the deviations of beam spin components from nominal values indicated that these were less than 5%.

B. The polarized target

The polarized proton target used in these experiments (PPT III) was built at Argonne. It consisted of a superconducting magnet whose field was in the horizontal plane and a target cryostat cooled by a ^{3}He refrigerator.

The magnet design was based on a similar magnet built at Saclay.[26,27] It consisted of pairs of superconducting Helmholtz coils which produced a 2.5-T field with a uniformity $|\Delta B/B| < 3\times10^{-4}$ in a spherical volume 4 cm in radius. In the S-type configuration, the aperture of the magnet allowed the detection of particles with angles as large as $\pm10°$ in the horizontal plane, or with angles between 42° and 138°.

The target cryostat was a horizontal continuous-flow ^{3}He refrigerator with ^{4}He precooling. The main ^{3}He pump was of the oil booster type,[28] which permitted operation at a ^{3}He temperature of ~0.4 K with a total target heat load of 30 mW. The total liquid-^{4}He consumption of the magnet and target cryostat was 10 l/hr.

Most of the measurements described in this paper were made with a pure S-type or a pure L-type target. However, small-angle measurements of C_{LL} could not be done with a pure L-type target because the target-magnet coils would interfere with the detection of the recoil protons. As a result, these data were taken with the target magnet rotated 18° relative to the nominal beam line. The recoil particles could then be detected in the 20° range between the coils or in the 96° aperture. On the other hand, this rotation caused mixing of the spin-spin correlation parameters measured (see Sec. IV).

The target material was ethylene glycol, doped with potassium dichromate and frozen in the form of $\sim$2-mm-diam spheres. The target length was 6.5, 8.0, and 8.0 cm for the S-type, pure L-type, and rotated L-type target configurations, respectively. The target material was enclosed in a FEP- (fluorinated ethylene propylene) Teflon container. The lateral target dimensions were 2.0 cm each. The density of the targets, exclusive of refrigerant, was estimated to be 0.81 ± 0.02 g/cm^3 based on measurements of other targets used by our group at the ZGS. The hydrogen nuclei were polarized by microwave dynamic nuclear cooling.[29] The computer-based nuclear-magnetic-resonance spectrometer system is described in Ref. 30. Typical target polarizations ranged from 80% to 90%.

C. Detectors

The detectors for this experiment consisted of scintillation counters and MWPC's to detect the beam, the forward, and the recoil particles. In addition, two lead-scintillator sandwich veto counters (AU, AD) were located immediately above and below the polarized target to help suppress inelastic triggers. Finally, a gas Cherenkov counter was used to reject pions in the magnetic spectrometer for the C_{LL} measurements at the largest angles. The construction and design of the electronics for the MWPC's has been described previously[30,31] and will only be briefly mentioned here.

1. Beam-line detectors

A summary of the dimensions and locations of the beam-line detectors is given in Table II (see also Fig. 2). The first scintillation counter S_0 was located immediately upstream of the LH_2 target near the first focus in the beam. Its signal was used for both the polarimeter and for the elastic-scattering trigger. A veto counter, BA_1, was mounted on the upstream end of the first solenoid in order to reject any beam particles that would strike the walls of the solenoids. It had a circular hole slightly smaller than the inside diameter of the solenoid. Scintillation counters S_1 and S_2 were split into two segments ($S1U$ and $S1D$, up and down halves; and $S2L$ and $S2R$, left and right halves) to assist in beam steering. The segmentation also permitted rejection of some events with two beam particles arriving at nearly the same time. The

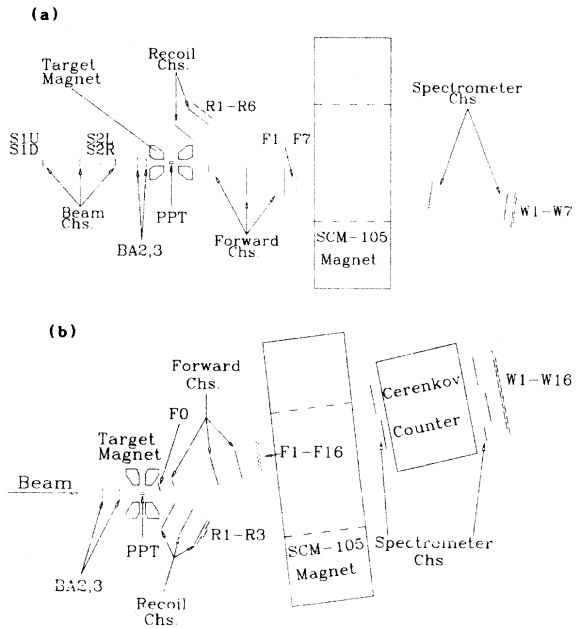

FIG. 2. Experimental layout showing the location of scintillation counters and MWPC's to detect the beam, scattered, and recoil protons. (a) Setup used during the small-angle data taking. (b) Setup used for C_{LL} measurements at the largest angles.

TABLE II. Beam-line detectors. Horizontal and vertical dimensions of the scintillation counters and MWPC's are listed. The distances upstream of the polarized target and scintillator thicknesses are also given. Each scintillator in BA_3 (BAL, BAR, BAU, BAD) was 14.0×6.4 cm^2 in area and 12.7 mm thick.

Detector designation	Horizontal dimension (cm)	Vertical dimension (cm)	Distance upstream of the PPT (m)	Other
S_0	7.62	7.62	~24.7	thickness=1.6 mm
BA_1	20.3	20.3	~12.2	thickness=6.4 mm hole diameter=8.9 cm
$S1U$, $S1D$	5.08	2.54	~2.95	thickness=3.2 mm
$MWPC_1$	12.8	12.8	2.57	64×64 wires
$MWPC_2$	12.8	12.8	1.83	64×64 wires
$S2L$, $S2R$	2.54	5.08	1.42	thickness=3.2 mm
$MWPC_3$	12.8	12.8	1.12	64×64 wires
BA_2	10.2	10.2	~0.68	thickness=9.5 mm hole diameter=2.54 cm
BA_3	14.0	14.0	~0.50	thickness=12.7 mm horizontal gap=14 mm vertical gap=16 mm

resolving time was about 12 ns, and such double beam events consisted of roughly 10% of all beam particles. However, a small fraction of the beam was lost in the narrow gap between the two halves of S_1 and S_2 caused by the wrapping of these counters. The scintillation counter BA_2 had a circular hole aligned on the beam axis and vetoed beam particles far from the nominal beam line. Finally, the segmented veto counter BA_3 consisted of four separate scintillation counters aligned to form a rectangular hole (14 mm horizontally by 16 mm vertically). Its main purpose was to reject any beam particles that would miss the polarized target. All of the above scintillation counters were heavily shielded from magnetic fields, especially near the polarized target.

For the C_{LL} measurements at the largest angles, scintillation counters S_0, S_1, and S_2 were not used because of the high beam rates (1.5–2.0×10^7 protons per pulse). Instead, the beam intensity was monitored by two scintillation-counter telescopes, each consisting of a pair of counters, viewing the target from above and below the beam.

In addition to the scintillation counters, three MWPC's were located in the beam to give information on the incident beam position and direction. Such information could have been used to improve the t resolution of the experiment for the smallest scattering angles. (Ultimately, events without signals from the beam MWPC's were included in the data sample, since the small $-t$ angular distributions for C_{SS}, C_{LS}, and C_{LL} were all featureless.) At larger scattering angles, the elastic-scattering rates were lower, which reduced the number of good events detected, and the beam rates were higher, which degraded the MWPC performance. Not only did electronics dead time reduce the chamber efficiency, but a buildup of silicon and oxygen compounds on the MWPC sense wires after long run periods with high voltage also decreased the efficiency. The sense wires in the direct beam required replacement after exposure to $\sim10^{10}$–10^{11} particles/cm^2, when the efficiency dropped below 90%. Consequently, these chambers were turned off for the largest scattering angle measurements when the beam rates were highest.

The MWPC's used in this experiment all had 20-μm gold-plated tungsten sense wires at a spacing of 2 mm and aluminized-Mylar or aluminum-foil high-voltage planes. The gap between the high-voltage plane and the sense wires was 0.64 cm. The gas mixture was 70% argon, 30% CO_2, and 0.5% freon 13-B1 and the operating voltage was 4400 V. A 100-ns gate was used to achieve good detection efficiency for all chambers in the experiment, with a minimum of accidentals or double-hit wires. Tests of other gas mixtures did not reduce the buildup of silicon and oxygen compounds on the sense wires.

The beam-line detectors were surveyed in place before the experiments. The relative alignment of various detectors and the polarized target was tested in a number of ways. The MWPC and scintillation-counter alignment was checked with the polarized target magnet on, using beam particles at low rates. The rates in the two segments of S_1 and of S_2 and the observed positions of the beam tracks in the MWPC's indicated that these detectors were aligned to better than ±1 mm. The beam was also used to verify the alignment with the polarized target. In this case, a special jig allowed tungsten rods to be accurately positioned midway between BA3L and BA3R and between BA3U and BA3D. Photographic film was positioned immediately downstream of the target cryostat in the direct beam. The beam position was adjusted to be centered on S_1 and S_2. After exposure to the beam, the relative position of the beam spot, the tungsten rods, and the target holder could be established (see Fig. 3). The target was normally adjusted to be within ±1–2 mm of the beam centerline as defined by the procedure above, and the tungsten rods were then removed.

2. *Recoil-proton detectors*

The recoil arm consisted of two or three MWPC's, each of which measured both a horizontal and a vertical posi-

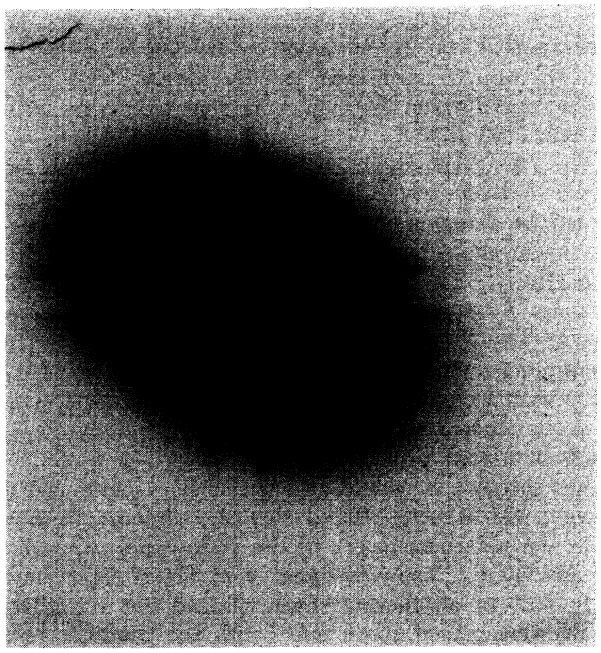

FIG. 3. Beam exposure photograph of the polarized-target container and the tungsten rods located between BA3L, BA3R and between BA3U, BA3D by the beam. The negative is shown for clarity. The NMR coils wrapped around the outside of the target appear as dots along the target sides.

tion, and a coarse scintillation hodoscope for triggering. These detectors were moved for each different angular region covered (low, medium, high $-t$ and 90° c.m. settings). They were optically surveyed after each move.

Two MWPC's were used in run 1, and three in run 2. The approximate distances to these chambers from the center of the polarized target were 61 and 100 cm in 1, and 62, 95, and 133 cm in 2. The active area of the chamber closest to the target was 25.6 cm vertical by 51.2 cm horizontal; the other chamber(s) was 51.2×51.2 cm^2 for all but the 90° c.m. setting. In the latter case, the dimensions of all three recoil chambers were 25.6 cm vertical by 51.2 cm horizontal. Since these MWPC's were in significant magnetic fields from the polarized target, and the energy of the recoil protons was low, corrections to the measured trajectories were needed. These corrections are described in Sec. III.

The recoil hodoscope consisted of four to six counters of 6.4-mm-thick plastic scintillator. It was located several cm behind the MWPC farthest from the target. Signals from these counters were used in the trigger and in the data analysis to remove spurious groups of wires in the MWPC's. The photomultipliers for these counters were heavily shielded from the polarized target magnetic field

3. *The magnetic spectrometer*

The forward-scattered proton was detected in a large-aperture magnetic spectrometer (see Fig. 2). The magnet aperture was 35 cm high by 213 cm wide, and the distance from the center of the polarized target to the center of the magnet was 366 cm in run 1 and 333 cm in run 2. The separation could not have been significantly reduced or there would have been damage to the polarized-target superconducting magnet. The central field of the analyzing magnet was ~1.87 T and the field integral through the magnet was about 1.65 T m. The magnet was centered on the nominal beam line in run 1 and rotated 7.2°, with the polarized target as pivot, during run 2.

The SCM-105 magnetic field was studied in several ways. A Hall probe was used to investigate fringe fields and to obtain the field at the magnet center as a function of magnet current. In addition, several hundred trajectories were measured with a floating-wire technique. These data were fit with a constant $\int B\,dl$ and a polynomial in terms of the position and angle before, and the position and angle after the magnet. A nine-term polynomial was eventually used which matched the measured momentum to $\pm0.35\%$, whereas the calculated spectrometer resolution was $\pm2\%$. Finally, a 267-cm-long flip coil with current integrator was used to measure $\int B\,dl$ for some trajectories as a check on the wire orbit results. The SCM-105 magnetic field was monitored continuously with a Hall probe during the experimental measurements.

Three MWPC's and a scintillation-counter hodoscope were mounted upstream of the analyzing magnet. The chambers measured both a horizontal and a vertical position. The active area of the chamber closest to the polarized target was 12.8×12.8 cm^2, and that of the other two was 25.6 cm vertical by 51.2 cm horizontal. The distances from the target to the three chambers were approximately 76, 153, and 229 (during run 1), or 203 cm (run 2). The seven elements of the hodoscope were 6.4 mm thick, 3.0 cm wide, and 21.6 cm high. Each element was viewed by a single Amperex XP1110 or PM1910 photomultiplier through a Lucite light guide. To change from one angular region to another, the three MWPC's did not need to move in general, but the hodoscope position had to be adjusted. Therefore, the scattering angle determination for all 1 runs was performed by the same chambers. For the 2 runs, the high $-t$ C_{SS} and low $-t$ C_{LL} data had the same MWPC positions, but the medium $-t$ C_{LL} positions were different.

Downstream of the analyzing magnet were two more MWPC's and a final scintillation-counter hodoscope. The chambers measured both a horizontal and a vertical position, and their active areas were 51.2×51.2 cm^2. They were located about 5.2 and 6.7 m from the polarized target. The seven elements of the hodoscope were 6.4 or 12.7 mm thick, 14.6 cm wide, and 53.3 cm high. Each element was viewed by two RCA 8575 or Amperex 56 AVP photomultipliers through adiabatic light guides. The chambers and hodoscope were rigidly mounted on a table that rolled on specially leveled rails; the table top could also rotate about a pivot relative to the rails. The chamber positions were surveyed for each angular region measured, and a typical setting change for the whole experiment took a few hours (excluding surveying) for all but the 90° c.m. setting.

The number of F and W hodoscope elements was increased from 7 to 16 and the number of MWPC's was also

increased for the 90° c.m. setting. The dimensions of the additional hodoscope elements were the same as those used for the other settings. Four of the MWPC's after the spectrometer magnet (SCM-105) had active areas 51.2×51.2 cm^2, and the fifth had an area 51.2 cm vertical by 25.6 cm horizontal. In addition, one of the large MWPC's closest to the SCM-105 was moved beam-right for some runs to extend the spectrometer acceptance to smaller angles.

A gas-filled Cherenkov counter was also installed for the 90° c.m. setting between the two sets of chambers after the analyzing magnet [see Fig. 2(b)]. The sensitive volume of this detector was approximately 190 cm wide, 61 cm high, and 152 cm along the beam. Thin aluminum sheet metal covered a frame of welded aluminum angle on all sides except the windows where the particles entered and exited. These windows were 0.13-mm Mylar covered with black cloth. Cherenkov light was reflected from a 3.2-mm-thick, 183×61-cm^2 cylindrical acrylic mirror and focused with Winston cones. Six Amperex XP2041 photomultipliers with a spacing of 30.5 cm detected the Cherenkov light. The gas used was freon-12 at one atmosphere, corresponding to a pion threshold of roughly 3.0 GeV/c. Tests with 2-GeV/c electrons and 5-GeV/c pions gave efficiencies $\geq 99\%$ for the electrons for five of the photomultipliers, and about 94% for the most beam-left tube, for all trajectories accepted in the experiment. For pions near threshold, the efficiency averaged about 90%.

D. Electronic logic

A diagram of the electronics is shown in Fig. 4 for most of the elastic-scattering measurements. A number of accidental coincidences were also measured, but they have been omitted from Fig. 4 for clarity. The good beam signal was defined by the coincidence BEAM$=S_0\cdot S_1\cdot S_2\cdot\overline{\text{BA}}$, where S_1 was a logical OR of $S1U$ and $S1D$, and similarly for S_2. The veto BA consisted of a logical OR of BA_1, BA_2, the four segments of BA_3, and the coincidence signals $S1U\cdot S1D$ and $S2L\cdot S2R$. Roughly 15—25% of the signals $S=S_0\cdot S_1\cdot S_2$ were rejected by BA in BEAM. The fraction depended on beam intensity, since the spot size was generally larger for high intensities; see Sec. II A. The signal T was BEAM vetoed by the computer busy signal. Computer dead time usually ranged from 5% to 15%, depending on the angular region covered, as well as the beam intensity.

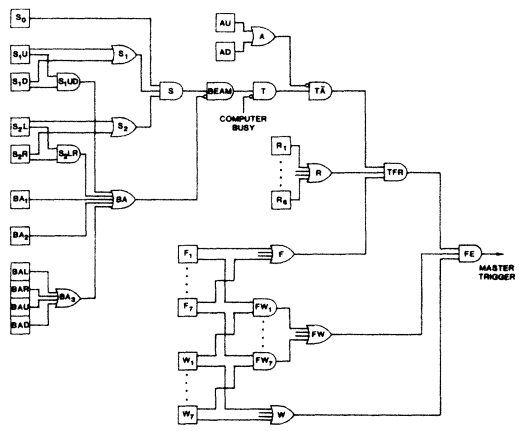

FIG. 4. Electronics logic diagram for the elastic-scattering trigger.

The fast event signal was defined by the coincidence FE$=T\cdot F\cdot W\cdot R\cdot$ FW$\cdot\overline{A}$, where F, W, and R were logical OR of the elements of the first and second hodoscopes in the spectrometer and the hodoscope in the recoil arm, respectively. The FW signal was a logical OR of coincidences $F_i\cdot W_i$ between the spectrometer hodoscope elements. The F hodoscope counters were adjacent but not overlapping, while the W hodoscope counters were staggered with a considerable overlap. These two hodoscopes were constructed and surveyed so that essentially all elastically scattered protons from the polarized target that passed through F_i would also strike W_i. (Note that the counter widths were 3.0 and 14.6 cm, while the distances from the polarized target to the hodoscopes were about 2.4 and 7.0 m.) The veto signal A contained two counters (AU, AD) of alternating sheets of lead and scintillator. These were placed above and below the polarized-target cryostat to reject inelastic events. At times, a veto counter AB1 was installed near the beam, on the side opposite to the events detected in the spectrometer, to further reduce the trigger rate. Typical ratios of FE/T were roughly 12, 3, and 1×10^{-5} for low, medium, and high $-t$ angular regions.

In the special case of the 90° setting, the coincidence $S=S_0\cdot S_1\cdot S_2$ was removed from the fast event trigger. Tests indicated essentially no change in the trigger rate or degradation of the elastic signal. This removal was required because the accidentals in S and BEAM were prohibitive at the intensity used for these measurements. The computer-busy, BA_1, BA_2, and BA_3 vetoes remained in the trigger. In addition, more F and W hodoscope elements and MWPC's were added to the electronics, and the Cherenkov counter signals were used as a veto.

E. Data acquisition

Information from the MWPC's and the hodoscope latches for each event was read into an EMI 6050 computer through CAMAC and then written onto tape. A variety of scalers and also the polarization of the target were similarly read at the end of each ZGS pulse. Between pulses, the computer analyzed some of the events to monitor the hardware performance. For example, the MWPC data were tested by histogramming the number of wires, the number of wire groups, and the number of hardware read-in errors per event. Histograms of the number of times each wire had a signal in each wire plane permitted bad electronic channels to be located. The latch-bit pattern and correlations between the F and W hodoscope latches were also displayed to check for dead counters or electronic problems in the trigger. Ratios of various scalers, and asymmetries in these ratios, were also computed. Many hardware problems were rapidly located as a result of these monitors of the performance of the apparatus during the many months of running for this experiment.

III. DATA ANALYSIS

This section describes a number of topics dealing with the data analysis. Several runs were used to check alignment constants for the chambers and to obtain the shadows of hodoscope elements on the MWPC's. Polarized-target magnetic-field corrections to the trajectories were required, and these are discussed. Distributions of kinematical quantities and a discussion of the cuts applied are also given.

At each angular setting, for each spin parameter measured, one or more runs were taken with the polarized-target magnet turned off. This permitted a test of the surveyed positions for the MWPC's, and it was particularly useful for the five chambers in the magnetic spectrometer. Generally, the positions of the three MWPC's between the polarized target and the analyzing magnet agreed with the survey to ± 1 mm. The chambers were important, since they defined the scattering angle and t of the events (the magnetic-field corrections of the forward trajectories were small because the momentum of the elastically scattered protons was high). The positions of the two MWPC's after the analyzing magnet and of the recoil MWPC's agreed with the surveyed values to roughly ± 5 mm. The chamber positions were adjusted to give straight lines that went through the center of the target on the average.

The determination of the hodoscope-counter shadows on the MWPC's was performed by calculation and by the use of data taken with all magnetic fields on. The approximate range of wires in each chamber that corresponded to a given hodoscope element (F, W, or R) was computed using survey information where available. This served as a cross-check, especially for the data that showed a steep angular dependence across the face of the chambers. From the actual data, the hodoscope-latch information was also used to find the appropriate range of wires; it was usually wider than the calculated range (from a combination of magnetic-field and target-size effects). For the actual data analysis, the adopted shadows were chosen to cover both the calculated and observed ranges of wires for each hodoscope element. The shadow information was used to remove spurious wires in the MWPC's for each event.

Corrections to the observed trajectories for the effects of the polarized-target magnetic fields were usually required for the beam and forward protons, as well as the recoil protons. The polarized-target magnetic field could be accurately calculated, since this superconducting magnet contained very little magnetizable iron, and since the coils formed sets of Helmholtz coil pairs. The predictions of a computer program that used details of the magnet construction to evaluate the magnetic field have been experimentally verified in special cases by actual field measurements of the magnet. Particle trajectories were numerically integrated through this computed magnetic field *assuming* they corresponded to elastically scattered or beam protons. Typically several hundred trajectories were computed for each angular setting. Polynomial fits in terms of the MWPC coordinates were made to the deviations of these trajectories from straight lines. These polynomial fits were used in the data analysis program to correct the observed trajectories to obtain angles and positions at the target center. For the beam particles, an average correction for the magnetic-field effects was computed and applied to all events. Especially for the S-type polarized-target data, these corrections had a dramatic effect on the coplanarity of the events (see Sec. IV).

Since the magnetic-field corrections were calculated assuming pp elastic scattering, inelastic events were improperly corrected, especially for the low-momentum recoil particles. As a consequence, some inelastics were rejected on the basis of target cuts. In effect, this procedure allowed the polarized-target magnet to be employed as an analyzing magnet as well.

For most of the elastic-scattering data, the minimum information required to reconstruct the event included (a) less than 20 wires and five groups of wires in each MWPC plane, (b) less than two F hodoscope counters latched or less than two wire groups in one of the front three MWPC's in the spectrometer, (c) less than two R hodoscope elements latched, or less than two wire groups in one of the recoil MWPC's, (d) only one good $F_i - W_i$ match (a typical event had one F element and two W elements latched, because of the staggered counters in the W hodoscope), (e) at least one recoil chamber with both horizontal and vertical position information, (f) at least two spectrometer chambers with vertical position information, and (g) at least three spectrometer chambers with horizontal position information with at least one of these before and one after the analyzing magnet. An additional requirement was imposed later in the analysis; either the forward or recoil chamber information was required to give a unique trajectory, while the other arm was required to give no more than two trajectories.

When these conditions were all satisfied, kinematic quantities were then computed for each event (after magnetic-field corrections). Very near the center of the target, the forward and recoil trajectories were taken to be roughly straight lines. The interaction point was assigned to be the midpoint of the shortest line segment connecting the forward and recoil trajectories, and the distance of closest approach (DCA) was the length of that line segment. Plots of the target x, y, and z coordinates and of DCA are shown in Fig. 5. (Here y is up, z is downstream along the beam, and x, y, z forms a right-handed coordinate system.) These results are shown before cuts, and the locations of the cuts are also given. Also shown in Fig. 5 are plots of the difference in target position as computed from the forward and recoil trajectories and as obtained from the beam chambers.

From the spectrometer chamber information, and the field integral fit, the missing mass was calculated assuming the target and detected particles were protons. Distributions of this quantity before cuts are shown in Fig. 6 for the low, medium, and high $-t$ settings. Cuts used in the final data analysis are indicated. The peaks near the proton mass contained quasielastic events from the nuclei in the polarized target as well as elastic events. The width includes contributions from multiple scattering, quasielastic kinematics, and the spectrometer momentum resolution [roughly $\pm(2-3)\%$ at 12 GeV/c].

The angle-angle correlation for pp elastic scattering was

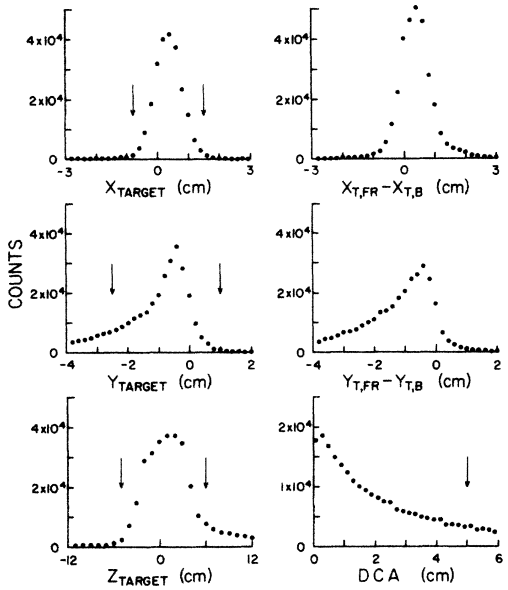

FIG. 5. Kinematic quantities computed from the medium $-t$ C_{LS} data. The interaction point defined by the forward and recoil trajectories is $(X_{\text{TARGET}}, Y_{\text{TARGET}}, Z_{\text{TARGET}})=(X_{T,FR}, Y_{T,FR}, Z_{T,FR})$, and the distance of the closest approach of the two trajectories is DCA. The difference in target position as obtained from the beam chambers ($X_{T,B}Y_{T,B}$ at $Z_{T,B}=0$) is also shown. Arrows denote the location of cuts applied to the data. The long tail on the Y_{TARGET} arises from magnetic-field corrections to inelastic events.

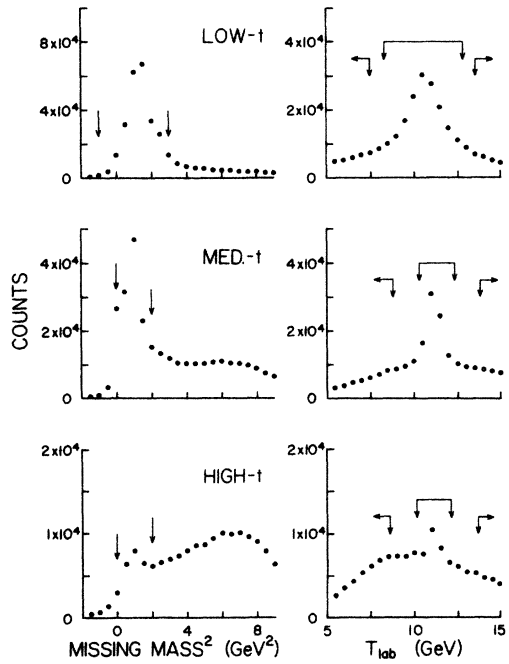

FIG. 6. The square of the missing mass and the quantity T_{lab} computed from Eq. (1) are shown before cuts for the low, medium, and high $-t$ C_{LS} data. Arrows around the peaks denote the location of cuts applied to the data. Additional arrows at high and low values of T_{lab} correspond to events used as "noncoplanar background."

imposed by making cuts on the quantity T_{lab} calculated from

$$\tan\theta_f\tan\theta_r=\frac{4m^2}{s}=\frac{1}{1+T_{\text{lab}}/2m}\ , \tag{1}$$

where θ_f and θ_r are the laboratory forward and recoil angles, T_{lab} is the laboratory kinetic energy of the beam, and m is the proton mass. Plots of the quantity T_{lab} are also shown in Fig. 6 before cuts. Two sets of cuts are given in Fig. 6, one for the "elastic" and one for the "background."

The final elastic signal was obtained after the cuts using the coplanarity distribution $(\phi_f-\phi_r-180°)$. Figure 7 shows several examples of the coplanarity for elastic and background events as defined by T_{lab}. After normalizing these two distributions in the wings, the true elastic events were found by subtraction. The asymmetries were then computed from

$$\epsilon=P_BP_T\tilde{C}_{\alpha\beta}=\frac{(I^{++}+I^{--})-(I^{+-}+I^{-+})}{(I^{++}+I^{--})+(I^{+-}+I^{-+})}\ , \tag{2}$$

where $I^{\pm\pm}=N^{\pm\pm}/T^{\pm\pm}$ and N^{+-} refers to the number of true elastic events corresponding to beam polarization in the $+\alpha$ direction and target polarization in the $-\beta$ direction, etc. The quantity T is the dead time corrected good beam as defined in Sec. II. The beam and target polarizations are P_B and P_T, respectively.

The procedure above was followed for each angular bin in θ_f. In addition, it was also performed for the sum of all bins at a given spectrometer setting for each run individually. The value of χ^2 per degree of freedom (χ^2/DF) using the average value from the elastic events was always near 1.0. Similarly, the asymmetries of the total back-

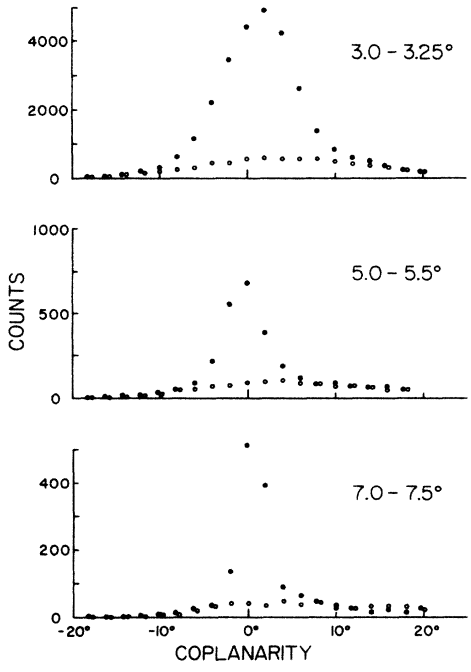

FIG. 7. Coplanarity distribution for "elastic" (solid circles) and "background" (open circles) for three laboratory angular bins for the C_{LS} data.

TABLE III. Events, beam, and time for each configuration. The total number of good incident beam protons is $\sum T$, the raw triggers read and written onto tape is $\sum$Read, and the approximate number of elastic events is $\sum$Elastics. The total data-taking time for each configuration is also shown.

Configuration	$\sum T$	$\sum$Read	$\sum$Elastics	No. of days
Low $-t$ C_{SS}	13×10^9	1.54×10^6	89×10^3	2
Medium $-t$ C_{SS}	94	2.65	108	5
High $-t$ C_{SS} (run 1)	28	0.36	1.5	2
(run 2)	161	1.97	6.8	7
Low $-t$ C_{LS}	19	2.62	176	3
Medium $-t$ C_{LS}	54	1.47	61	4
High $-t$ C_{LS}	148	1.17	9.8	9
Low $-t$ C_{LL}	37	2.81	409	4
Medium $-t$ C_{LL}	199	5.73	175	9
90° C_{LL}		24.2	6.5	32

ground counts were consistent with zero within statistical uncertainties.

IV. RESULTS

A summary of total run times, the summed T values, the events written on tape, and the number of elastic events is given in Table III for each angular setting. The measured parameters $\tilde{C}_{\alpha\beta}$ are also tabulated as a function of θ_f in Table IV for each setting. Since the angular regions had a considerable overlap, a check is permitted on the consistency of the results. From Table IV it can be seen that the agreement of data between different settings is consistent with the quoted statistical errors.

The quantities $\tilde{C}_{\alpha\beta}$ given in Table IV are not pure spin-spin correlation parameters in general. One effect that must be taken into account is the alteration of the effective scattering plane by the polarized-target magnetic field. For the S-type target runs, the beam and outgoing protons were deflected downward by the polarized-target magnetic field, but the detectors were centered on the nominal beam elevation. Since the recoil detectors essentially determined the acceptance of the experiment, the effective scattering plane was changed from the horizontal. During the data analysis, histograms were made of the spherical coordinates θ_f, ϕ_f of the events after cuts and after magnetic-field corrections. From these it was possible to compute the mixture of components during the $\tilde{C}_{LS}$ and $\tilde{C}_{SS}$ data-taking periods.

For two of the $\tilde{C}_{LL}$ angular regions, the polarized-target magnetic field was rotated 18° from the nominal beam line. This was necessary because of the interference of the target magnet coils with the desired acceptance; even with the rotation, some reduction of acceptance occurred. The rotation caused an even more severe mixing of spin parameters than for $\tilde{C}_{LS}$ or $\tilde{C}_{SS}$. For the 90° C_{LL} setting, the beam and target were purely L type, and no mixing of spin components occurred.

The polarized-target magnetic field affected not only the trajectories, but also the beam spin in some cases. This obviously affected the low and medium $-t$ settings for C_{LL} because of the rotated polarized-target magnetic field. For the $\tilde{C}_{LS}$ results, the S-type target would precess the N- and L-type beam spin components. During most runs, the beam-line solenoid currents were adjusted to give a mixture of N- and L-type beam spin before the target, so that nearly pure L-type beam was present at the target center (taking into account the alteration of the effective

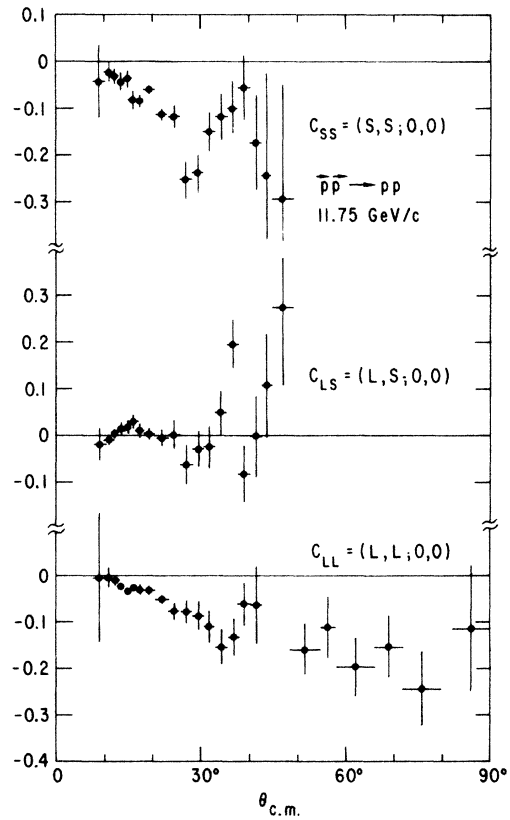

FIG. 8. Pure spin-spin correlation parameters C_{SS}, $C_{LS}=C_{SL}$, and C_{LL} as measured by this experiment for pp elastic scattering at 11.75-GeV/c laboratory beam momentum. Data from all settings have been combined and corrected for the presence of other spin parameters as described in the text.

TABLE IV. Measured spin-spin correlation parameters at 11.75 GeV/c. No corrections have been applied for mixing of spin parameters (see Sec. IV). The errors quoted are statistical only; there is an additional systematic uncertainty of ±7% for the absolute beam and target polarizations.

(a) $\tilde{C}_{SS}$

θ_{lab}	Low $-t$	Medium $-t$	High $-t$ (run 1)	High $-t$ (run 2)
1.5–2.0°	−0.043±0.078			
2.0–2.25°	−0.023±0.021			
2.25–2.5°	−0.031±0.017			
2.5–2.75°	−0.043±0.017			
2.75–3.0°	−0.036±0.019			
3.0–3.25°	−0.078±0.021	−0.342±0.212		
3.25–3.5°	−0.081±0.027	−0.083±0.017		
3.5–4.0°	−0.038±0.030	−0.062±0.008		
4.0–4.5°	−0.073±0.049	−0.114±0.014		
4.5–5.0°	−0.000±0.089	−0.125±0.026		
5.0–5.5°	−0.260±0.140	−0.243±0.042	−0.283±0.159	−0.296±0.151
5.5–6.0°	+0.027±0.216	−0.274±0.061	−0.186±0.105	−0.233±0.059
6.0–6.5°		−0.086±0.070	−0.331±0.148	−0.162±0.056
6.5–7.0°		−0.138±0.076	−0.181±0.154	−0.081±0.070
7.0–7.5°		−0.162±0.087	+0.032±0.158	−0.075±0.080
7.5–8.0°		+0.036±0.105	−0.032±0.185	−0.146±0.102
8.0–8.5°		−0.091±0.159	−0.279±0.252	−0.200±0.148
8.5–9.0°			−0.296±0.278	−0.154±0.335
9.0–10.0°			−0.175±0.340	−0.401±0.339

(b) $\tilde{C}_{LS}$

θ_{lab}	Low $-t$	Medium $-t$	High $-t$
1.5–2.0°	−0.024±0.035		
2.0–2.25°	−0.014±0.014		
2.25–2.5°	−0.001±0.012		
2.5–2.75°	+0.008±0.013		
2.75–3.0°	+0.013±0.014		
3.0–3.25°	+0.020±0.014	+0.097±0.130	
3.25–3.5°	−0.022±0.018	+0.049±0.023	
3.5–4.0°	+0.013±0.022	+0.000±0.012	
4.0–4.5°	−0.053±0.038	+0.006±0.020	
4.5–5.0°	−0.070±0.055	+0.027±0.034	
5.0–5.5°	−0.180±0.094	−0.020±0.061	−0.071±0.071
5.5–6.0°	−0.138±0.180	−0.013±0.089	−0.035±0.040
6.0–6.5°		+0.037±0.108	−0.045±0.051
6.5–7.0°		+0.093±0.111	+0.032±0.051
7.0–7.5°		+0.224±0.129	+0.182±0.056
7.5–8.0°		−0.046±0.166	−0.092±0.063
8.0–8.5°		−0.178±0.269	+0.004±0.089
8.5–9.0°			+0.091±0.109
9.0–10.0°			+0.252±0.160

(c) $\tilde{C}_{LL}$

θ_{lab}	Low $-t$	Medium $-t$	90°
1.5–2.0°	−0.012±0.130		
2.0–2.25°	−0.009±0.018		
2.25–2.5°	−0.009±0.008		
2.5–2.75°	−0.019±0.006		
2.75–3.0°	−0.027±0.007		
3.0–3.25°	−0.017±0.008		
3.25–3.5°	−0.027±0.010		
3.5–4.0°	−0.026±0.010	−0.036±0.011	
4.0–4.5°	−0.040±0.019	−0.056±0.007	
4.5–5.0°	+0.010±0.060	−0.077±0.012	
5.0–5.5°	−0.255±0.232	−0.093±0.018	
5.5–6.0°		−0.095±0.027	

TABLE IV. (*Continued*).

	(c) $\tilde{C}_{LL}$		
θ_{lab}	Low $-t$	Medium $-t$	90°
6.0–6.5°		−0.114±0.029	
6.5–7.0°		−0.132±0.032	
7.0–7.5°		−0.064±0.034	
7.5–8.0°		−0.086±0.039	
8.0–8.5°		−0.063±0.074	
9.75–11.25°			−0.159±0.055
11.25–12.0°			−0.112±0.065
12.0–14.0°			−0.198±0.062
14.0–15.5°			−0.153±0.065
15.5–17.75°			−0.244±0.080
18.5–21.0°			−0.115±0.135

scattering plane). However, at times one of the solenoids was not operational. In that case, the beam was a mixture of N- and L-type spin at the target. Some corrections have already been applied for this effect to the data in Table IV (C_{NS} and C_{NL} are both zero from parity conservation). Table V summarizes the mixing of spin-spin correlation parameters for the data in Table IV.

Pure spin-spin correlation parameters could be obtained from the measurements of $\tilde{C}_{\alpha\beta}$ using C_{NN} results from Refs. 4–9. First pure C_{SS} was obtained, since no C_{LS} or C_{LL} contributions were present in the $\tilde{C}_{SS}$ data. Then C_{LS} and finally C_{LL} were obtained. The pure parameters are listed in Table VI and are shown in Fig. 8. The C_{NN} and P data of Refs. 1–9 are given in Fig. 9.

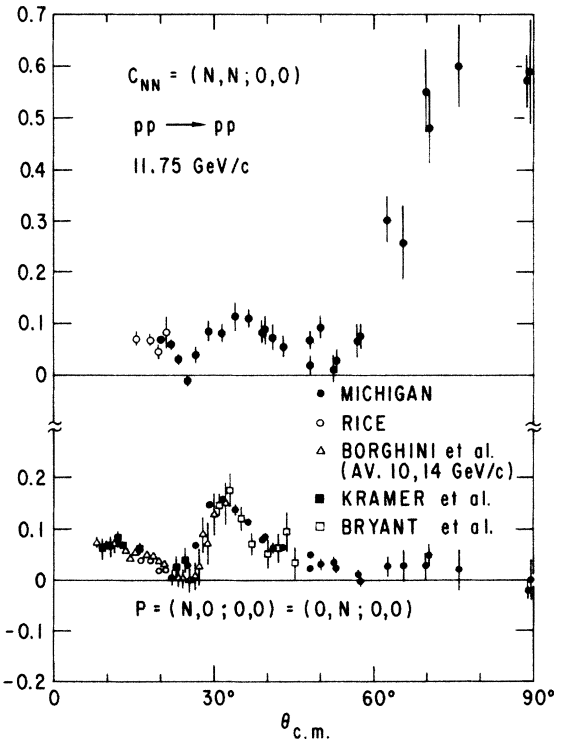

FIG. 9. Spin parameters C_{NN} and polarization P for pp elastic scattering at 11.75 GeV/c from Refs. 1–9. The Rice results are preliminary.

For the values in Tables IV and VI, the total systematic error is ±7%. It consists of (a) ±5.2% for the absolute beam polarization,[14] (b) ±4% for the absolute target polarization, and (c) ±2.3% for knowledge of the spin direction. The third contribution corresponds to an estimated ±4° uncertainty in spin direction from the spin precession in various bending magnets and knowledge of the incoming beam spin direction (the polarimeter measured only one component of the beam spin). In addition to these systematic errors, there is an additional estimated uncertainty of ±0.04° in the absolute laboratory scattering angle θ_f. Since the beam chamber information was not required for all the data, the angular resolution is ±0.18° from the measured beam divergence (Table I) and multiple-scattering effects after the beam MWPC's to the center of the target.

V. INTERPRETATION

A. Model-independent analysis

The following amplitudes[32] will be used:

$$\begin{aligned}
\phi_s &= (\phi_1 - \phi_2)/2 \,, \\
\phi_t &= (\phi_1 + \phi_2)/2 \,, \\
\phi_T &= (\phi_3 - \phi_4)/2 \,, \\
\phi_\tau &= (\phi_3 + \phi_4)/2 \,, \\
\phi_5 &= \phi_5 \,.
\end{aligned} \tag{3}$$

These are defined in terms of the helicity amplitudes ϕ_1–ϕ_5 of Jacob and Wick[33] and Goldberger, Grisaru, MacDowell, and Wong.[34] The amplitude ϕ_s contains only spin-singlet contributions; ϕ_T and ϕ_τ contain only spin-triplet partial waves and ϕ_t and ϕ_5 contain only coupled spin-triplet terms. These amplitudes are the same as the H-spin amplitudes.[35]

The following relations were derived in Ref. 32:

TABLE V. Mixing of spin parameters. This table gives the mixture of true spin-spin correlation parameters for the measurements in Table IV. Where a range of values appears, the first value corresponds to the smallest forward-scattering angle and the second to the largest angle at that angular setting.

Setting	Components			
	C_{NN}	C_{SS}	C_{LS}	C_{LL}
Low $-t$ C_{SS}	0.01—0.03	0.99—0.97	0.00	0.00
Medium $-t$ C_{SS}	0.01—0.02	0.99—0.98	0.00	0.00
High $-t$ C_{SS} (runs 1 and 2)	0.00—0.02	1.00—0.98	0.00	0.00
Low $-t$ C_{LS}	−(0.04—0.07)	0.04—0.07	1.00—0.99	0.00
Medium $-t$ C_{LS}	0.00	0.00	1.00—0.99	0.00
High $-t$ C_{LS}	−(0.03—0.05)	0.03—0.05	1.00—0.99	0.00
Low $-t$ C_{LL}	−0.01	0.01	0.32	0.946
Medium $-t$ C_{LL}	−0.01	0.01	0.32	0.946
90° C_{LL}	0.00	0.00	0.00	1.00

$$
\begin{aligned}
|\phi_s|^2&=(1-C_{NN}-C_{SS}-C_{LL})(d\sigma/d\Omega)/4\ ,\\
|\phi_\tau|^2&=(1-C_{NN}+C_{SS}+C_{LL})(d\sigma/d\Omega)/4\ ,\\
|\phi_t|^2+|\phi_5|^2&=(1+C_{NN}+C_{SS}-C_{LL})(d\sigma/d\Omega)/4\ ,\\
|\phi_T|^2+|\phi_5|^2&=(1+C_{NN}-C_{SS}+C_{LL})(d\sigma/d\Omega)/4\ .
\end{aligned}
\tag{4}
$$

Also, the real and imaginary parts of one combination of amplitudes can be obtained

$$
\phi_t^*\phi_5-\phi_T\phi_5^*=(C_{LS}+iP)(d\sigma/d\Omega)/2\ . \tag{5}
$$

The square root of the quantities in Eq. (4) are shown in Fig. 10. The amplitudes have been normalized so that the differential cross section is unity,

TABLE VI. Pure spin-spin correlation parameters at 11.75 GeV/c. This table gives the corrected spin-spin correlation parameters. Weighted averages of results from different spectrometer angle settings are given, and the errors quoted are statistical only. There is an additional systematic uncertainty of ±7% for the absolute beam and target polarizations and the mixing of spin parameters.

θ_{lab}	$-t$ [(GeV/c)^2]	$\theta_{c.m.}$	$p_T{}^2$ [(GeV/c)^2]	C_{SS}	C_{LS}	C_{LL}
1.5 — 2.0°	0.09— 0.17	7.8—10.4°	0.09—0.17	−0.043±0.078	−0.019±0.035	−0.005±0.137
2.0 — 2.25°	0.17— 0.21	10.4—11.7°	0.17—0.21	−0.023±0.021	−0.010±0.014	−0.005±0.019
2.25— 2.5°	0.21— 0.26	11.7—13.0°	0.21—0.26	−0.031±0.017	+0.003±0.012	−0.010±0.008
2.5 — 2.75°	0.26— 0.31	13.0—14.3°	0.26—0.31	−0.044±0.017	+0.014±0.013	−0.024±0.007
2.75— 3.0°	0.31— 0.37	14.3—15.5°	0.31—0.36	−0.038±0.019	+0.018±0.014	−0.034±0.008
3.0 — 3.25°	0.37— 0.44	15.5—16.8°	0.36—0.43	−0.084±0.021	+0.029±0.014	−0.027±0.009
3.25— 3.5°	0.44— 0.50	16.8—18.1°	0.43—0.49	−0.085±0.014	+0.011±0.014	−0.031±0.011
3.5 — 4.0°	0.50— 0.65	18.1—20.6°	0.49—0.63	−0.061±0.008	+0.005±0.011	−0.033±0.008
4.0 — 4.5	0.65— 0.82	20.6—23.2°	0.63—0.79	−0.113±0.013	−0.005±0.018	−0.053±0.009
4.5 — 5.0°	0.82— 1.00	23.2—25.7°	0.79—0.96	−0.117±0.025	+0.003±0.029	−0.077±0.016
5.0 — 5.5°	1.00— 1.20	25.7—28.2°	0.96—1.13	−0.253±0.038	−0.062±0.042	−0.078±0.023
5.5 — 6.0°	1.20— 1.42	28.2—30.6°	1.13—1.32	−0.238±0.039	−0.027±0.036	−0.089±0.031
6.0 — 6.5°	1.42— 1.65	30.6—33.1°	1.32—1.51	−0.150±0.042	−0.025±0.046	−0.111±0.034
6.5 — 7.0°	1.65— 1.89	33.1—35.5°	1.51—1.71	−0.118±0.050	+0.050±0.046	−0.155±0.037
7.0 — 7.5°	1.89— 2.14	35.5—37.8°	1.71—1.92	−0.099±0.056	+0.196±0.051	−0.132±0.040
7.5 — 8.0°	2.14— 2.40	37.8—40.2°	1.92—2.12	−0.056±0.069	−0.082±0.060	−0.063±0.046
8.0 — 8.5°	2.40— 2.68	40.2—42.5°	2.12—2.33	−0.174±0.101	−0.003±0.085	−0.064±0.083
8.5 — 9.0°	2.68— 2.96	42.5—44.8°	2.33—2.53	−0.244±0.218	+0.107±0.110	
9.0 —10.0°	2.96— 3.54	44.8—49.3°	2.53—2.93	−0.295±0.245	+0.272±0.162	
9.75—11.25°	3.40— 4.31	48.2—54.8°	2.83—3.40			−0.159±0.055
11.25—12.0°	4.31— 4.78	54.8—57.9°	3.40—3.66			−0.112±0.065
12.0 —14.0°	4.78— 6.04	57.9—66.0°	3.66—4.25			−0.198±0.062
14.0 —15.50°	6.04— 6.98	66.0—71.7°	4.25—4.59			−0.153±0.065
15.5 —17.75°	6.98— 8.35	71.7—79.6°	4.59—4.92			−0.244±0.080
18.5 —21.0°	8.79—10.18	82.1—90.0°	4.99—5.09			−0.115±0.135

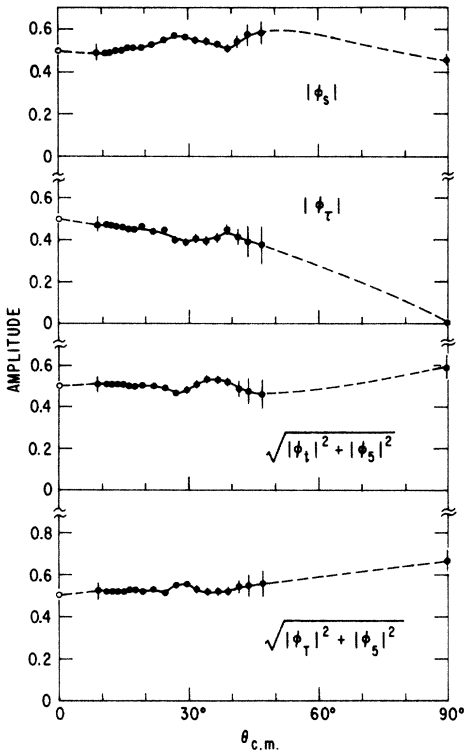

FIG. 10. Magnitudes of the amplitudes from Eqs. (3) and (4) for pp elastic scattering at 11.75 GeV/c. The open circles at 0° correspond to the assumption of N_0 dominance as described in the text. The 90° values are obtained from C_{NN} and C_{LL} data, since ϕ_τ and ϕ_5 vanish there. The lines are hand drawn.

$$d\sigma/d\Omega = 1 = |\phi_s|^2 + |\phi_t|^2 + |\phi_T|^2 + |\phi_\tau|^2 + 2|\phi_5|^2 . \tag{6}$$

Some structure is apparent in all four quantities in Fig. 10, especially beyond 25°.

At small angles and high energy, diffraction dominates pp elastic scattering. In terms of the t-channel-exchange amplitudes,[36,37] the dominant amplitude is

$$N_0 = (\phi_1 + \phi_3)/2 = (\phi_s + \phi_t + \phi_T + \phi_\tau)/2 \tag{7}$$

and all other amplitudes are very small.[25,38–41] As a consequence, it is expected that ϕ_s, ϕ_t, ϕ_T, and ϕ_τ will all be roughly equal in both magnitude and direction, while $\phi_5 \to 0$ as $\theta_{c.m.} \to 0$ because of helicity conservation. With the normalization adopted in Eq. (6), the magnitudes should be 0.5 at 0°; this result is shown as open circles in Fig. 10. In fact, the four quantities in Fig. 10 are near 0.5 over the full angular range $\theta_{c.m.} \sim 10°–50°$.

An attempt was made to place limits on the magnitudes of ϕ_t, ϕ_T, and ϕ_5 from the data. However, there are four bilinear equations in these amplitudes [the second two relations in Eq. (4), and the real and imaginary parts of Eq. (5)], but there are five unknown real numbers to be determined (an overall phase cannot be measured) corresponding to the three complex amplitudes. In general, the three magnitudes are bounded above by Eq. (4), but they can go down to zero. The only exception is for ϕ_5, whose lower bound is determined by the magnitude of the polarization P, which is nonzero at most angles. Assigning the arbitrary phase so that ϕ_5 is purely real, then some possible solutions for ϕ_5, ϕ_t, and ϕ_T are shown in Fig. 11 for several values of the magnitude of ϕ_5 and of $\theta_{c.m.}$. In general, none of the amplitudes vanishes and the amplitudes have significantly different phases.

At angles beyond $\theta_{c.m.} \sim 50°$, the only available pp elastic-scattering spin data at this energy are P, C_{NN}, and C_{LL} (see Figs. 8 and 9). At $\theta_{c.m.} = 90°$, the amplitudes ϕ_5 and ϕ_τ vanish,[32] which leads to the well-known relation

$$C_{NN} - C_{SS} - C_{LL} = 1 . \tag{8}$$

By solving this equation for C_{SS} and substituting in Eq. (4), the magnitudes of ϕ_s, ϕ_t, and ϕ_T can be obtained. The results are plotted in Fig. 10. From Eq. (8) and the condition $|C_{ij}| \leq 1$, the following conditions apply at $\theta_{c.m.} = 90°$:

$$\begin{aligned} &C_{NN} \geq C_{LL} , \\ &C_{NN} \geq C_{SS} , \\ &-C_{LL} \geq C_{SS} . \end{aligned} \tag{9}$$

The numerical values of the measured quantities C_{NN} and C_{LL} and of the derived parameter C_{SS} are consistent with these conditions.

At angles other than 90°, some limits can be placed on the quantities in Eq. (4). The requirement that the four expressions in Eq. (4) must all give non-negative quantities yields the relation

$$1 - |C_{NN} + C_{LL}| \geq C_{SS} \geq |C_{NN} - C_{LL}| - 1 . \tag{10}$$

For $\theta_{c.m.} \sim 70°–90°$, the value of C_{NN} is large, which places a significant constraint on the range of allowed C_{SS} values. Solving these numerically leads to

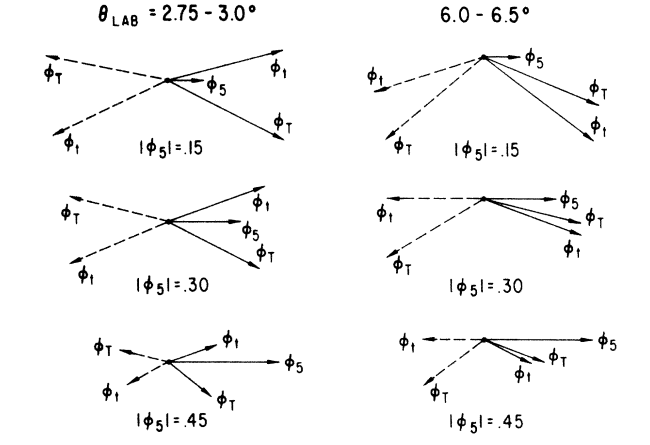

FIG. 11. Possible solutions for the phases and magnitudes of ϕ_t, ϕ_T, and ϕ_5 for two angular bins and three values of $|\phi_5|$ for pp elastic scattering at 11.75 GeV/c. The amplitude ϕ_5 is taken to be purely real and positive. Two solutions for each θ_{lab} and $|\phi_5|$ are shown, corresponding to a discrete ambiguity in the amplitude determination.

$$
\begin{aligned}
&0.5 \gtrsim |\phi_s| \geq 0 , \\
&0.5 \gtrsim |\phi_\tau| \geq 0 , \\
&0.8 \gtrsim (|\phi_t|^2 + |\phi_5|^2)^{1/2} \gtrsim 0.5 , \\
&0.7 \gtrsim (|\phi_T|^2 + |\phi_5|^2)^{1/2} \gtrsim 0.4 ,
\end{aligned}
\tag{11}
$$

in the range $\theta_{\text{c.m.}} \sim 70°$–$90°$. It can be seen that these are consistent with the 90° values derived above.

In the angular range between about 50° and 90°, the following equations, derived from Eq. (4), give some information on the amplitudes responsible for the observed change in C_{NN} (Fig. 9):

$$
\begin{aligned}
&|\phi_t|^2 + |\phi_5|^2 - |\phi_\tau|^2 = (C_{NN} - C_{LL})(d\sigma/d\Omega)/2 , \\
&|\phi_T|^2 + |\phi_5|^2 - |\phi_s|^2 = (C_{NN} + C_{LL})(d\sigma/d\Omega)/2 .
\end{aligned}
\tag{12}
$$

The quantities $(C_{NN} \pm C_{LL})/2$ are plotted in Fig. 12. Structure in both arises from the structure in C_{NN}, since C_{LL} is relatively slowly varying over the full angular range. As noted before, both ϕ_τ and ϕ_5 vanish as $\theta_{\text{c.m.}} \to 90°$, and $|\phi_s|$ is only slightly less at 90° than at 50°. Therefore, the structure in Fig. 12 near 65° may arise from an increase in magnitude of both ϕ_t and ϕ_T, or a combination of effects from all five amplitudes. Additional understanding of the structure in C_{NN} requires measurements of other spin parameters between 50° and 90°.

In particular, since measurements of the spin of an outgoing proton are difficult at these energies and angles (the *pp* elastic-scattering cross section is small, and the *pp* or *pC* analyzing power for the second scattering is also small), the only two spin parameters that could easily be measured in addition to P, C_{NN}, and C_{LL} are C_{LS} and C_{SS}. It can be seen from Fig. 8 that C_{LS} is consistent with zero over the full angular range measured, except possibly for one point. Also $P \simeq 0$ beyond 50°, so both may vanish at larger angles. On the basis of Eq. (5), it

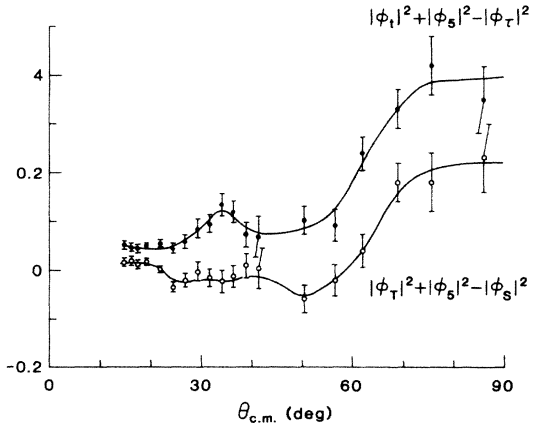

FIG. 12. The quantities $(C_{NN} - C_{LL})/2 = |\phi_t|^2 + |\phi_5|^2 - |\phi_\tau|^2$ and $(C_{NN} + C_{LL})/2 = |\phi_T|^2 + |\phi_5|^2 - |\phi_s|^2$ for *pp* elastic scattering at 11.75 GeV/c as a function of c.m. angle. At $\theta_{\text{c.m.}} = 90°$, the amplitudes ϕ_5 and ϕ_τ vanish. The lines shown are hand drawn.

can be shown that if $C_{LS} = 0$ and $P = 0$ at some angle, then either $\phi_5 = 0$ or $|\phi_t| = |\phi_T|$. In the first case, the magnitude of all five amplitudes could be obtained. In the second case, Eq. (4) implies $C_{LL} = C_{SS}$ (conversely, if $C_{LL} = C_{SS}$ and $P = 0$, then $C_{LS} = 0$). In conclusion, measurements of C_{LS} and C_{SS} for $\theta_{\text{c.m.}} = 50°$–$90°$ could considerably improve the understanding of the structure observed in C_{NN} near 65°. Such measurements are feasible, but might well entail a mixing of spin observables more severe than that experienced for C_{LL} in this experiment.

B. Comparison to theoretical models

There are two regions where the data can be compared to theoretical models, at small angles ($-t \lesssim 0.8$ GeV$^2/c^2$) and near $\theta_{\text{c.m.}} = 90°$. In the first case, the N_0 amplitude [Eq. (7)] is expected to be dominant, whereas all others are to be small. In terms of the t-channel-exchange amplitudes[36,37]

$$
\begin{aligned}
&N_1 = \phi_5 , \\
&N_2 = (\phi_4 - \phi_2)/2 , \\
&U_0 = (\phi_1 - \phi_3)/2 , \\
&U_2 = (\phi_4 + \phi_2)/2 ,
\end{aligned}
\tag{13}
$$

the spin parameters measured at 11.75 GeV/c can be expressed as

$$
\begin{aligned}
1 = d\sigma/d\Omega &= |N_0|^2 + 2|N_1|^2 + |N_2|^2 \\
&\quad + |U_0|^2 + |U_2|^2 \\
&\simeq |N_0|^2 , \\
P\, d\sigma/d\Omega &\simeq -2\,\text{Im}(N_0 N_1^*) , \\
C_{NN} d\sigma/d\Omega &\simeq -2\,\text{Re}(N_0 U_2^*) , \\
C_{SS} d\sigma/d\Omega &\simeq +2\,\text{Re}(N_0 U_2^*) , \\
C_{LS} d\sigma/d\Omega &\simeq 0 , \\
C_{LL} d\sigma/d\Omega &\simeq -2\,\text{Re}(N_0 U_0^*) .
\end{aligned}
\tag{14}
$$

Terms quadratic in the small amplitudes have been neglected. In addition, as the energy is increased, the magnitudes of N_1, N_2, U_0, and U_2 at small $|t|$ are expected to decrease relative to N_0.

From Fig. 8 it can be seen that $C_{LS} \simeq 0$, as expected from Eq. (14). This is also true at considerably lower energies.[42] A comparison of P, C_{NN}, C_{SS}, and C_{LL} at 6 and 11.75 GeV/c from Refs. 1, 3, 4, 9, 18, 19, 22, and 43–47 is shown in Fig. 13. The energy dependences of P, C_{SS}, and C_{LL} are considerably different. Between 6 and 11.75 GeV/c, P drops by a factor of roughly 2 at the smallest $|t|$ and by larger factors at larger angles. The magnitude of C_{SS} also drops by roughly a factor of 2 for $|t| \lesssim 0.4$ GeV$^2/c^2$, but there is less energy dependence at larger $|t|$. Finally, the magnitude of C_{LL} at 11.75 GeV/c is comparable to, or larger than at 6 GeV/c for $-t \simeq 0.2$–0.8 GeV$^2/c^2$. The size of the statistical uncertainties on the data, and the quite small magnitude of C_{LL}, make it difficult to draw more definitive conclusions on the energy dependence.

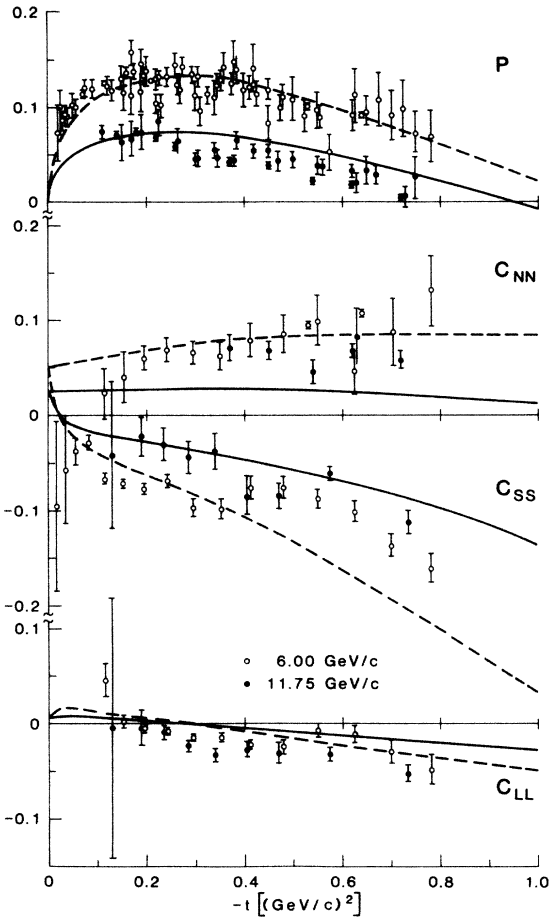

FIG. 13. A comparison of pp elastic-scattering spin parameters P, C_{NN}, C_{SS}, and C_{LL} at beam momenta of 6.0 and 11.75 GeV/c as a function of four-momentum transfer squared. The 6-GeV/c data for P are from Refs. 18 and 43–47; for C_{NN} are from Refs. 18 and 47; for C_{SS} are from Ref. 19; and for C_{LL} are from Ref. 22. The 11.75-GeV/c data for P are from Refs. 1, 3, 4, and 9; for C_{NN} are from Refs. 4 and 9; and for C_{SS} and C_{LL} are from this experiment. The data from Ref. 9 are preliminary. The solid and dashed curves correspond to predictions from Ref. 38 at 11.75 and 6 GeV/c, respectively.

According to the Regge exchange analysis of Ref. 38, it is expected that the magnitudes of P, C_{SS}, and C_{LL} at small $|t|$ will decrease between 6 and 11.75 GeV/c. The predictions from the improved model [Eq. (35)] of Ref. 38 are compared with data in Fig. 13. The magnitudes, signs, t, and s dependences of P and C_{SS} are in quite good agreement. There are some differences between data and theoretical expectations for C_{NN} and C_{LL}, principally in the energy dependence.

At large $\theta_{\text{c.m.}}$, there has been a variety of attempts to model the rapid change of C_{NN} with angle (Refs. 6–8 and Fig. 9). These include calculations based on the quark-parton model,[48–54] and several phenomenological models.[55–57] An early attempt to predict pp elastic-scattering spin observables, before the 11.75-GeV/c C_{NN} data were taken, used a pure vector-type quark-quark interaction.[48] This model disagrees with $C_{NN}(90°)$ above 10 GeV/c.

Perturbative QCD and constituent-interchange models of nucleon-nucleon elastic scattering have been studied by Farrar, Gottlieb, Sivers, and Thomas,[49] Brodsky, Carlson, and Lipkin,[50] Szwed,[51] Wolters,[52] and Anselmino.[53] In general, the assumptions of constituent exchange and helicity conservation at $\theta_{\text{c.m.}}=90°$ lead to the predictions

$$C_{NN}=-C_{LL}=-C_{SS}=\tfrac{1}{3}\ , \tag{15}$$

in disagreement with the data in Figs. 8 and 9.

If it is assumed that valence quarks carry all the proton helicity, and that quark helicity is conserved (massless quarks), then

$$\phi_2=\phi_5=0 \tag{16}$$

at all angles. This implies

$$\begin{aligned}&\phi_s=\phi_t\ ,\\ &C_{NN}=-C_{SS}\ .\end{aligned} \tag{17}$$

From Eq. (4),

$$\begin{aligned}&|\phi_s|^2=|\phi_t|^2=(1-C_{LL})(d\sigma/d\Omega)/4\ ,\\ &|\phi_\tau|^2=(1-2C_{NN}+C_{LL})(d\sigma/d\Omega)/4\ ,\\ &|\phi_T|^2=(1+2C_{NN}+C_{LL})(d\sigma/d\Omega)/4\ .\end{aligned} \tag{18}$$

The data can be used to test for consistency with Eq. (16). Figure 10 shows that there are differences between ϕ_s and ϕ_t, or that ϕ_5 is nonzero up to $\theta_{\text{c.m.}}\sim 50°$ or $-t\simeq 4$ GeV$^2/c^2$. Above $\theta_{\text{c.m.}}\sim 50°$, Eq. (11) indicates $|\phi_s|^2=|\phi_t|^2\simeq 0.25$ is allowed, whereas Eq. (18) would give a value of about 0.29 ± 0.02. Moreover, as shown in Figs. 8 and 9, $P\simeq 0$ at large angles, and $C_{LS}\simeq 0$ at all angles. These are consistent with the condition $\phi_5=0$. Finally, the requirement that $|\phi_\tau|^2$ is non-negative gives the following condition for $\theta_{\text{c.m.}}\geq 65°$:

$$(1-2C_{NN}+C_{LL})/4=-(0.072\pm 0.020)\geq 0\ . \tag{19}$$

At exactly 90°, ϕ_τ vanishes and the equality should hold in Eq. (19). In that case, the experimental value is $-(0.066\pm 0.040)$. The conclusion is that the data at 11.75 GeV/c are marginally consistent with a dynamics in which the dominant amplitudes at large angle obey quark-helicity conservation with the valence quarks carrying all the proton helicity.

As noted above, additions or changes are needed to the pure quark-interchange amplitudes in order to understand the large values of C_{NN} near 90°. These have included the additions of instantons[49] and Landshoff pinch singularities,[50] and changes in the frame for quark-helicity conservation[51] or in the quark recombination mechanism.[53] The predictions of Anselmino[53] for $C_{NN}(\theta)$ and $C_{LL}(\theta)$ are roughly correct, whereas discrepancies of at least three standard deviations occur for the predictions of Refs. 49–51.

On the other hand, it is not clear that either the incident-beam energy or the momentum transfer is high enough for perturbative QCD to apply. In particular,

Isgur and Llewellyn Smith[58] suggest that perturbative QCD cannot be applied to pp elastic scattering until both the energy and the momentum transfer are many orders of magnitude higher than in the present experiment.

A somewhat different approach is used by Preparata and Soffer,[54] who employ the massive-quark model to predict C_{LL} and C_{NN}. Although the agreement with $C_{LL}(90°)$ and with large angle C_{NN} is fairly good, the angular dependence of C_{LL} at smaller angles disagrees with the data by several standard deviations. Similarly, Avilez, Cocho, and Moreno[56] dismiss perturbative QCD and perform a phenomenological analysis of nucleon-nucleon elastic-scattering data from 3 to 12 GeV/c. Their analysis finds that correlations between quarks are important. Their predictions are approximately correct for C_{LL} near 60°, but the angular distribution does not agree with the data. Finally, Arash, Moravcsik, and Goldstein[57] have analyzed pp elastic scattering in terms of planar-transverse amplitudes and find a simple pattern at $\theta_{\text{c.m.}}=90°$. On this basis, they predict $C_{LL}(90°)\sim+0.3$, which differs from the measured value by about three standard deviations.

Another feature of the data that has received considerable theoretical interest concerns the behavior of pp elastic scattering at fixed c.m. angle (usually 90°) as a function of beam momentum. The differential cross-section data are not completely featureless, but rather show an oscillatory behavior superimposed on a steeply falling exponential in p_T or power law in s, (Refs. 59–63). As shown in Fig. 14, the behavior of $C_{NN}(90°)$ shows large changes with beam momentum,[8,18,64,65] between 2 and 13 GeV/c which are discussed by Arash, Moravcsik, and Goldstein[57] and compared to the cross section variations by Wolters[52] and Hendry.[55]

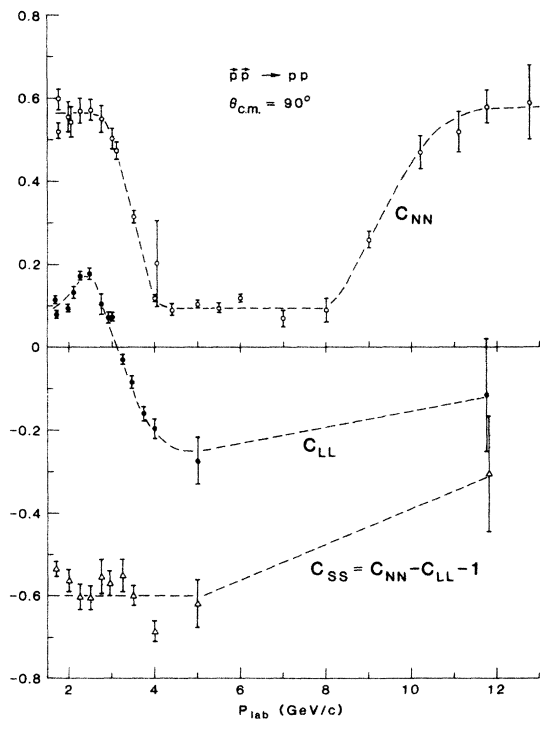

FIG. 14. Plots of $\theta_{\text{c.m.}}=90°$ pp elastic-scattering spin parameters C_{NN}, C_{LL}, and C_{SS} as a function of beam momentum. The C_{NN} results are from Refs. 8, 18, 64, and 65 and the C_{LL} data from Refs. 24, 66, and this experiment. The values of C_{SS} were obtained from the C_{NN} and C_{LL} data using Eq. (8). The lines shown are hand drawn.

Large changes in $C_{LL}(90°)$ are also observed.[24,66] These data, and the values of $C_{SS}(90°)$ obtained from Eq. (8), are shown in Fig. 14. The large drop in C_{NN} is seen to be accompanied by a corresponding drop in C_{LL}, so that C_{SS} is roughly constant. The lack of C_{LL} or C_{SS} data at 90° between 5 and 11.75 GeV/c and the statistical precision of $C_{LL}(90°)$ at 11.75 GeV/c do not permit conclusions on whether C_{LL} is constant, or C_{SS} is constant, or both vary in this energy range.

VI. CONCLUSIONS

New measurements of three spin parameters C_{SS}, C_{LS}, and C_{LL} for pp elastic scattering at 11.75 GeV/c are presented. The parameter C_{LS} is consistent with zero over the full angular range measured, but both C_{SS} and C_{LL} show significant spin effects for $\theta_{\text{c.m.}}\gtrsim 20°$ or $-t\gtrsim 0.6$ GeV$^2/c^2$ (Fig. 8).

The magnitudes of the amplitudes in Eqs. (3) and (4) are shown in Fig. 10. In general, all five amplitudes are nonzero, and all the quantities in Fig. 10 exhibit variations with angle in the range $\theta_{\text{c.m.}}=20°$–$50°$. The amplitudes ϕ_5, ϕ_t, and ϕ_T generally have significantly different phases in this angular range (Fig. 11). It is not possible on the basis of the existing data above $\theta_{\text{c.m.}}=50°$ (P, C_{NN}, C_{LL}) to clarify which amplitude causes the rise in C_{NN} near $\theta_{\text{c.m.}}\approx 65°$.

A comparison of pp elastic-scattering data at 6 and 11.75 GeV/c for $-t=0$–0.8 GeV$^2/c^2$ shows considerably different behavior for P, C_{SS}, and C_{LL} (Fig. 13). As expected theoretically,[38] there is a significant drop in P at higher energies over this t range and for the magnitude of C_{SS} at $|t|\lesssim 0.4$ GeV$^2/c^2$. However, little energy variation is seen for C_{LL} or for C_{SS} at $-t=0.4$–0.8 GeV$^2/c^2$.

The assumptions that valence quarks carry all the proton helicity and that quark helicity is conserved (massless quarks) lead to the conditions $\phi_2=\phi_5=0$ (Refs. 49 and 50). Tests of these conditions show marginal agreement for $\theta_{\text{c.m.}}\gtrsim 65°$, where C_{NN} is large. Perhaps components of the proton wave function other than valence quarks carry some of the proton helicity.

The theoretical predictions of Anselmino[53] show the best agreement to the C_{NN} and C_{LL} data at large angles. Predictions by Brodsky, Carlson, and Lipkin,[50] Preparata and Soffer,[54] Avilez, Cocho, and Moreno,[56] and Arash, Moravcsik, and Goldstein[57] are several standard deviations different from the measurements. However, questions have been raised about the applicability of perturbative QCD (used in Refs. 49–53) to exclusive processes.[58] Beam momenta and momentum transfers orders of magnitude higher than those in this experiment may be required for pp elastic scattering.

Finally, an oscillatory behavior in $C_{LL}(90°)$ with beam momentum is consistent with the data (Fig. 14). This behavior may be related to oscillations in $d\sigma/dt(90°)$

about a steeply falling exponential in p_T or power law in s, and also oscillations in $C_{NN}(90°)$ (Refs. 52, 55, 57, and 59—64). The interpretation of this behavior at 90° is not presently clear.

ACKNOWLEDGMENTS

It is a pleasure to acknowledge the technical efforts of R. Daly, O. Fletcher, W. Haberichter, R. Johnson, T. Kasprzyk, R. Miller, F. Paulis, A. Rask, and L. Rupert for their assistance with the construction of the experiment and operation of the polarized target. We also wish to thank Dr. E. Berger, Dr. D. Sivers, Dr. H. Lipkin, and other members of the Argonne High Energy Physics Division theory group and Dr. S. Brodsky for many useful discussions; J. Blakely and I. McMackin for their help with the Cherenkov counter construction; and the staff of the Zero Gradient Synchrotron accelerator for their assistance throughout this experiment. We wish to especially thank Dr. E. Berger for a careful reading of the manuscript and for assistance with the theoretical predictions from Ref. 38. This work was supported by the U.S. Department of Energy, Division of High Energy Physics, Contract No. W-31-109-ENG-38.

---

[a]Present address: Bell Communications Research, Redbank, NJ 07701

[b]Present address: Los Alamos National Laboratory, Los Alamos, NM 87545.

[c]Present address: Naval Weapons Center, China Lake, CA 93555.

[d]Present address: University of Chicago Medical Center, Box 440, 5041 South Maryland Ave., Chicago, IL 60637.

[e]Present address: Kyoto University, Kyoto 606, Japan.

[f]Present address: Service S.P.R., Bldg. 24, Saclay Nuclear Center, 91191 Saclay, France.

[g]Present address: University of Pennsylvania, Philadelphia, PA 19174.

[h]Present address: IBM Japan, Ltd. Mori Bldg. 21, 4-34 Roppongi 1 Chrome, Minato-ku, Tokyo 106, Japan.

[i]Present address: KEK, Tsukuba, Ibaraki 305, Japan.

[1]M. Borghini, L. Dick, J. C. Olivier, H. Aoi, D. Cronenberger, G. Gregoire, Z. Janout, K. Kuroda, A. Michalowicz, M. Poulet, D. Sillou, G. Bellettini, P. L. Braccini, T. Del Prete, L. Fao, P. Laurelli, G. Sanguinetti, and M. Valdata, Phys. Lett. **36B**, 501 (1971).

[2]G. W. Bryant, M. Corcoran, R. R. Crittenden, S. W. Gray, R. M. Heinz, H. A. Neal, and D. R. Rust, Phys. Rev. D **13**, 1 (1976).

[3]S. L. Kramer, D. S. Ayres, D. Cohen, R. Diebold, A. J. Pawlicki, and A. B. Wicklund, Phys. Rev. D **17**, 1709 (1978).

[4]K. Abe, R. C. Fernow, T. A. Mulera, K. M. Terwilliger, W. DeBoer, A. D. Krisch, H. E. Miettinen, J. R. O'Fallon, and L. G. Ratner, Phys. Lett. **63B**, 239 (1976).

[5]H. E. Miettinen, K. Abe, R. C. Fernow, A. D. Krisch, T. A. Mulera, A. J. Salthouse, B. Sandler, K. M. Terwilliger, J. R. O'Fallon, L. G. Ratner, and P. F. Schultz, Phys. Rev. D **16**, 549 (1977).

[6]J. R. O'Fallon, L. G. Ratner, P. F. Schultz, K. Abe, R. C. Fernow, A. D. Krisch, T. A. Mulera, A. J. Salthouse, B. Sandler, K. M. Terwilliger, D. G. Crabb, and P. H. Hansen, Phys. Rev. Lett. **39**, 733 (1977).

[7]D. G. Crabb, R. C. Fernow, P. H. Hansen, A. D. Krisch, A. J. Salthouse, B. Sandler, K. M. Terwilliger, J. R. O'Fallon, E. A. Crosbie, L. G. Ratner, and P. F. Schultz, Phys. Rev. Lett. **41**, 1257 (1978).

[8]E. A. Crosbie, L. G. Ratner, P. F. Schultz, J. R. O'Fallon, D. G. Crabb, R. C. Fernow, P. H. Hansen, A. D. Krisch, A. J. Salthouse, B. Sandler, T. Shima, K. M. Terwilliger, N. L. Karmakar, S. L. Linn, A. Perlmutter, and P. Kyberd, Phys. Rev. D **23**, 600 (1981).

[9]J. Lesikar (private communication), preliminary Rice data.

[10]I. P. Auer, E. Colton, W. R. Ditzler, D. Hill, H. Spinka, N. Tamura, J.-J. Tavernier, G. Theodosiou, K. Toshioka, D. Underwood, R. Wagner, and A. Yokosawa, Phys. Rev. Lett. **52**, 808 (1984).

[11]T. Khoe, R. L. Kustom, R. L. Martin, E. F. Parker, C. W. Potts, L. G. Ratner, R. E. Timm, A. D. Krisch, J. B. Roberts, and J. R. O'Fallon, Part. Accel. **6**, 213 (1975).

[12]E. F. Parker, L. G. Ratner, B. C. Brown, S. W. Gray, A. D. Krisch, H. E. Miettinen, J. B. Roberts, and J. R. O'Fallon, Phys. Rev. Lett. **31**, 783 (1973).

[13]A. Lin, J. R. O'Fallon, L. G. Ratner, P. F. Schultz, K. Abe, D. G. Crabb, R. C. Fernow, A. D. Krisch, A. J. Salthouse, B. Sandler, and K. M. Terwilliger, Phys. Lett. **74B**, 273 (1978).

[14]H. Spinka, E. Colton, W. R. Ditzler, H. Halpern, K. Imai, R. Stanek, N. Tamura, G. Theodosiou, K. Toshioka, D. Underwood, R. Wagner, Y. Watanabe, A. Yokosawa, G. R. Burleson, W. B. Cottingame, S. J. Greene, S. Stuart, and J. J. Jarmer, Nucl. Instrum. Methods **211**, 239 (1983).

[15]E. P. Colton, IEEE Trans. Nucl. Sci. **NS-26**, 3206 (1979).

[16]E. Colton, I. P. Auer, A. Beretvas, D. Hill, K. Nield, B. Sandler, H. Spinka, D. Underwood, Y. Watanabe, and A. Yokosawa, Nucl. Instrum. Methods **151**, 85 (1978).

[17]E. Colton and D. R. Moffett, Nucl. Instrum. Methods **146**, 593 (1977).

[18]D. Miller, C. Wilson, R. Giese, D. Hill, K. Nield, P. Rynes, B. Sandler, and A. Yokosawa, Phys. Rev. Lett. **36**, 763 (1976); Phys. Rev. D **16**, 2016 (1977).

[19]I. P. Auer, D. Hill, R. C. Miller, K. Nield, B. Sandler, Y. Watanabe, A. Yokosawa, A. Beretvas, D. Miller, and C. Wilson, Phys. Rev. Lett. **37**, 1727 (1976).

[20]A. Beretvas, D. Miller, I. P. Auer, R. Giese, D. Hill, K. Nield, P. Rynes, B. Sandler, Y. Watanabe, and A. Yokosawa, Phys. Rev. D **20**, 21 (1979).

[21]I. P. Auer, E. Colton, D. Hill, K. Nield, B. Sandler, H. Spinka, Y. Watanabe, A. Yokosawa, and A. Beretvas, Phys. Lett. **67B**, 113 (1977).

[22]I. P. Auer, A. Beretvas, E. Colton, D. Hill, K. Nield, H. Spinka, D. Underwood, Y. Watanabe, and A. Yokosawa, Phys. Lett. **70B**, 475 (1977).

[23]I. P. Auer, E. Colton, H. Halpern, D. Hill, H. Spinka, G. Theodosiou, D. Underwood, Y. Watanabe, and A. Yokosawa, Phys. Rev. Lett. **41**, 354 (1978).

[24]I. P. Auer, A. Beretvas, E. Colton, H. Halpern, D. Hill, K. Nield, B. Sandler, H. Spinka, G. Theodosiou, D. Underwood, Y. Watanabe, and A. Yokosawa, Phys. Rev. Lett. **41**, 1436 (1978).

[25]I. P. Auer, J. Chalmers, E. Colton, R. Giese, H. Halpern, D.

Hill, R. Miller, K. Nield, B. Sandler, H. Spinka, N. Tamura, D. Underwood, Y. Watanabe, A. Yokosawa, A. Beretvas, and D. Miller, Phys. Rev. D **32**, 1609 (1985).

[26]P. Autones, J. C. Brisson, A. Boucherie, G. Cozzika, J. Deregel, J. P. Duthil, H. Desportes, Y. Ducros, A. Katz, A. deLesquen, J. P. Merlo, J. F. Mougel, J. Movchet, J. C. Raoul, B. Tsai, L. van Rossum, B. Amblard, J. M. Fontaine, M. Hansroul, and J. M. Rieubland, Nucl. Instrum. Methods **103**, 211 (1972).

[27]J. C. Raoul, P. Autones, R. Auzolle, C. Bruneton, J. Bystricky, G. Cozzika, J. Deregel, Y. Ducros, A. Gaidot, A. Katz, F. Khantine-Langlois, F. Lehar, A. deLesquen, J. P. Merlo, S. Miyashita, J. Movchet, J. Pierrard, M. Ramadier, P. Roubeau, G. Souchere, L. van Rossum, A. A. Derevschikov, N. I. Golovnya, Yu. S. Khoderev, Yu. A. Matulenko, A. P. Meschanin, S. B. Nurushev, A. I. Saraykin, V. S. Seleznev, V. V. Siksin, E. V. Smirnov, V. L. Solovyanov, V. N. Zapolsky, Yu. M. Kazarinov, M. Yu. Kazarinov, B. A. Khatchaturov, I. K. Potashnikova, and V. P. Kanavets, Nucl. Instrum. Methods **125**, 585 (1975).

[28]Manufactured by Edwards High Vacuum, Ltd., Grand Island, NY 14072, Model No. 18B4A.

[29]A. Abragam and M. Goldman, Rep. Prog. Phys. **41**, 395 (1978).

[30]I. P. Auer, D. Bridges, T. Droege, D. Hill, R. Giese, R. Miller, K. Nield, P. Rynes, B. Sandler, A. Yokosawa, G. Hicks, D. Miller, and C. Wilson, Phys. Rev. D **24**, 1771 (1981).

[31]K. Nield and R. Daly, Argonne National Laboratory Report No. ANL-HEP-PR-77-32, 1977 (unpublished).

[32]H. Spinka, Phys. Rev. D **30**, 1461 (1984).

[33]M. Jacob and G. C. Wick, Ann. Phys. (N.Y.) **7**, 404 (1959).

[34]M. L. Goldberger, M. T. Grisaru, S. W. MacDowell, and D. Y. Wong, Phys. Rev. **120**, 2250 (1960).

[35]H. Lipkin (private communication).

[36]E. Leader and R. Slansky, Phys. Rev. **148**, 1491 (1966); E. Leader, *ibid.* **166**, 1599 (1968).

[37]F. Halzen and G. H. Thomas, Phys. Rev. D **10**, 344 (1974).

[38]E. L. Berger, A. C. Irving, and C. Sorensen, Phys. Rev. D **17**, 2971 (1978); **23**, 2807(E) (1981).

[39]P. Kroll, E. Leader, and W. von Schlippe, J. Phys. G **4**, 1003 (1978).

[40]S. Wakaizumi and M. Sawamoto, Prog. Theor. Phys. **64**, 1699 (1980); S. Wakaizumi, *ibid.* **67**, 531 (1982).

[41]M. Matsuda, H. Suemitsu, W. Watari, and M. Yonezawa, Prog. Theor. Phys. **62**, 1436 (1979); **64**, 1344 (1980).

[42]I. P. Auer, E. Colton, W. R. Ditzler, D. Hill, R. Miller, H. Spinka, G. Theodosiou, J.-J. Tavernier, N. Tamura, K. Toshioka, D. Underwood, R. Wagner, A. Yokosawa, P. Kroll, and W. Jauch, Phys. Rev. Lett. **51**, 1411 (1983); **51**, 1814(E) (1983).

[43]M. Borghini, G. Coignet, L. Dick, K. Kuroda, L. DiLella, P. C. Macq, A. Michalowicz, and J. C. Olivier, Phys. Lett. **24B**, 77 (1966); M. Broghini, L. Dick, L. DiLella, A. Navarro, J. C. Olivier, K. Reibel, C. Coignet, D. Cronenberger, G. Gregoire, K. Kuroda, A. Michalowicz, M. Poulet, D. Sillou, C. Bellettini, P. L. Braccini, T. DelPrete, L. Foa, G. Sanguinetti, and M. Valdata, *ibid.* **31B**, 405 (1970).

[44]R. Diebold, D. S. Ayres, S. L. Kramer, A. J. Pawlicki, and A. B. Wicklund, Phys. Rev. Lett. **35**, 632 (1975).

[45]D. R. Rust, R. R. Crittenden, R. M. Heinz, H. A. Neal, I. Ambats, D. S. Ayres, R. Diebold, R. J. Jost, S. L. Kramer, W. T. Meyer, A. J. Pawlicki, C. E. W. Ward, A. B. Wicklund, A. Lesnik, D. M. Schwartz, and E. C. Swallow, Phys. Lett. **58B**, 114 (1975).

[46]R. D. Klem, H. W. Courant, J. Lee, M. L. Marshak, E. A. Peterson, K. Ruddick, T. Walsh, W. H. Dragoset, and J. B. Roberts, Phys. Rev. D **15**, 602 (1977).

[47]J. R. O'Fallon, E. F. Parker, L. G. Ratner, R. C. Fernow, S. W. Gray, A. D. Krisch, H. E. Miettinen, and J. B. Roberts, Phys. Rev. Lett. **32**, 77 (1974); R. C. Fernow, S. W. Gray, A. D. Krisch, H. E. Miettinen, J. B. Roberts, K. M. Terwilliger, W. deBoer, E. F. Parker, L. G. Ratner, and J. R. O'Fallon, Phys. Lett. **52B**, 243 (1974); L. G. Ratner, M. Borghini, W. deBoer, R. C. Fernow, A. D. Krisch, H. E. Miettinen, T. A. Mulera, J. B. Roberts, K. M. Terwilliger, and J. R. O'Fallon, Phys. Rev. D **15**, 604 (1977); M. Borghini, W. deBoer, R. C. Fernow, A. D. Krisch, H. E. Miettinen, T. A. Mulera, J. B. Roberts, K. M. Terwilliger, J. R. O'Fallon, and L. G. Ratner, *ibid.* **17**, 24 (1978).

[48]C. K. Chen, Phys. Rev. Lett. **41**, 1440 (1978).

[49]G. R. Farrar, S. Gottlieb, D. Sivers, and G. H. Thomas, Phys. Rev. D **20**, 202 (1979).

[50]S. J. Brodsky, C. E. Carlson, and H. Lipkin, Phys. Rev. D **20**, 2278 (1979).

[51]J. Szwed, Phys. Lett. **93B**, 485 (1980); Phys. Rev. D **25**, 735 (1982); Nucl. Phys. **B229**, 53 (1983).

[52]G. F. Wolters, Phys. Rev. Lett. **45**, 776 (1980).

[53]M. Anselmino, Z. Phys. C **13**, 63 (1982).

[54]G. Preparata and J. Soffer, Phys. Lett. **86B**, 304 (1979).

[55]A. W. Hendry, Phys. Rev. D **23**, 2075 (1981).

[56]C. Avilez, G. Cocho, and M. Moreno, Phys. Rev. D **24**, 634 (1981).

[57]F. Arash, M. J. Moravcsik, and G. R. Goldstein, Phys. Rev. D **31**, 667 (1985).

[58]N. Isgur and C. H. Llewellyn Smith, Phys. Rev. Lett. **52**, 1080 (1984).

[59]C. W. Akerlof, R. H. Hieber, A. D. Krisch, K. W. Edwards, L. G. Ratner, and K. Ruddick, Phys. Rev. **159**, 1138 (1967).

[60]R. C. Kammerud, B. B. Brabson, R. R. Crittenden, R. M. Heinz, H. A. Neal, H. W. Paik, and R. A. Sidwell, Phys. Rev. D **4**, 1309 (1971).

[61]A. W. Hendry, Phys. Rev. D **10**, 2300 (1974).

[62]B. Schrempp and F. Schrempp, Phys. Lett. **55B**, 303 (1975).

[63]B. Pire and J. P. Ralston, Phys. Lett. **117B**, 233 (1982); J. P. Ralston and B. Pire, Phys. Rev. Lett. **49**, 1605 (1982).

[64]D. A. Bell, J. A. Buchanan, M. M. Calkin, J. M. Clement, W. H. Dragoset, M. Furic, K. A. Johns. J. D. Lesikar, H. E. Miettinen, T. A. Mulera, G. S. Mutchler, G. C. Phillips, J. B. Roberts, and S. E. Turpin, Phys. Lett. **94B**, 310 (1980).

[65]A. Lin, J. R. O'Fallon, L. G. Ratner, P. F. Schultz, K. Abe, D. G. Crabb, R. C. Fernow, A. D. Krisch, A. J. Salthouse, B. Sandler, and K. M. Terwilliger, Phys. Lett. **74B**, 273 (1978).

[66]I. P. Auer, C. Chang-Fang, E. Colton, H. Halpern, D. Hill, H. Kanada, H. Spinka, N. Tamura, G. Theodosiou, K. Toshioka, D. Underwood, R. Wagner, and A. Yokosawa, Phys. Rev. Lett. **48**, 1150 (1982).

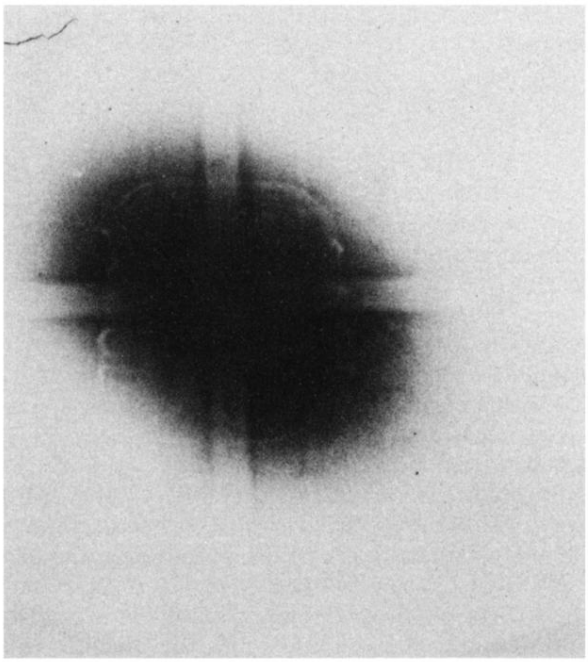

FIG. 3. Beam exposure photograph of the polarized-target container and the tungsten rods located between BA3L, BA3R and between BA3U, BA3D by the beam. The negative is shown for clarity. The NMR coils wrapped around the outside of the target appear as dots along the target sides.